On the average shape of the largest waves in finite water depths

Ioannis Karmpadakis* and Chris Swan

Department of Civil and Environmental Engineering, Imperial College London, London, UK

**Corresponding author address:* Ioannis Karmpadakis, Department of Civil and Environmental Engineering, Imperial College London, SW7 2AZ, London, UK.

E-mail: i.karmpadakis@imperial.ac.uk

ABSTRACT

This paper investigates the average shape of the largest waves arising in finite water depths. Specifically, the largest waves recorded in time-histories of the water surface elevation at a single point have been examined. These are compared to commonly applied theories in engineering and oceanographic practice. To achieve this both field observations and a new set of laboratory measurements are considered. The latter concern long random simulations of directionally spread sea-states generated using realistic JONSWAP frequency spectra. It is shown that approximations related to the linear theory of Quasi-Determinism (QD) cannot describe some key characteristics of the largest waves. While second-order corrections to the QD predictions provide an improvement, key effects arising in very steep or shallow water sea-states are not captured. While studies involving idealised wave groups have demonstrated significant changes arising as a result of higher-order nonlinear wave-wave interactions, these have not been observed in random sea-states. The present paper addresses this discrepancy by decomposing random wave measurements into separate populations of breaking and non-breaking waves. The characteristics of average wave shapes in the two populations are examined and their key differences discussed. These explain the mismatch between findings in earlier random and deterministic wave studies.

1. Introduction

The largest waves in the ocean have long attracted oceanographic and engineering interest. Regarding offshore and coastal structures, both the size and the shape of these waves represent key design parameters. For example, jacket-type structures require a deck elevation that is high enough to avoid potentially catastrophic wave-in-deck loading (Ma and Swan 2020). In principle, it is the largest waves, or waves with a very low probability of exceedance in a severe sea-state, that will give rise to this type of loading. These are typically defined by the integration of the short-term crest height distribution over the long term distribution of sea-state parameters (DNV 2010); the latter typically based on hindcast models.

Following this approach, a "design" wave is fitted to the required crest elevation and the wave kinematics calculated. These are then used to perform wave loading calculations; an essential part for any structural design. Traditionally, these "design" waves were defined using regular wave theories. More correctly, they should represent asymptotic approximations to random wave theories. In adopting this approach, very long random wave testing can be substituted by the investigation of selected wave events; the latter commonly defined by the theory of Quasi-Determinism (QD) following (Lindgren 1972; Boccotti 1983; Tromans et al. 1991).

The justification for using representative wave events has been extensively examined in the literature. Typically, the assessment involves comparisons between the average shape of (random) measured surface elevation time-histories and available analytical theories; broad agreement being generally reported (Phillips et al. 1993b; Jonathan and Taylor 1997; Tayfun and Fedele 2007). However, when one of these analytical representations is used as the input to a study of idealised wave groups in a fully nonlinear (numerical or experimental) simulation, different results arise. This refers to significant changes in the magnitude and symmetry (both vertical and horizontal) of the fully nonlinear waves (Johannessen and Swan 2001, 2003; Gibbs and Taylor 2005; Gibson et al. 2007; Adcock et al. 2015). This apparent discrepancy raises a number of important questions: Are these nonlinear effects important in random seas? If they are, why are they not observed in the average shape of the largest waves recorded therein?

Considering the statistical distribution of crest heights, several studies have illustrated that higher-order nonlinearities can play an important role (Onorato et al. 2009; Shemer et al. 2010). More importantly, recent results by Latheef and Swan (2013) and Karmpadakis et al. (2019) have shown that the competing mechanisms of nonlinear amplifications and wave breaking have a profound effect on crest height statistics. To illustrate this effect, the distribution of crest heights (η_c) normalised by their significant wave height (H_s) is shown on Figure 1. These results relate to a very steep, laboratory-generated, short-crested sea-state with $H_s = 15.3\,\mathrm{m}$ and effective water depth $k_p d = 1.22$ reported by Karmpadakis et al. (2019). The measured data are compared to the predictions of the commonly applied Forristall (2000) distribution. The latter is defined by:

$$Q = \exp\left[-\frac{1}{\alpha_F}\left(\frac{\eta_c}{H_s}\right)^{\beta}_{F}\right], \tag{1}$$

where α_F and β_F are the scale and shape coefficients defined in terms of the sea-state steepness and Ursell parameter and Q is the probability of exceedance. The Forristall (2000) distribution was derived as a fit to second-order numerical simulations. In comparing the measured data with the second-order distribution, two important observations can be made. First, nonlinear amplifications (beyond second-order) are present, appearing as increases above the Forristall distribution in the range: $10^{-3} < Q < 10^{-1}$. Second, in the tail of the distribution the largest crest heights fall below the Forristall distribution. This demonstrates the dissipative effects of wave breaking for $Q < 10^{-3}$. Taken together, these two competing effects have a profound influence on the crest height distribution and have important design implications.

Building upon these observations of the crest heights, the present paper addresses the questions raised above concerning the significance of nonlinear amplifications and wave breaking on the average shape of the largest waves. To achieve this, experimental measurements are supplemented by field and numerical data, the intention being to examine the characteristics of non-breaking and breaking waves separately. The contents of this paper are arranged as follows. First, a brief overview of relevant work in the field is provided in Section 2. The adopted methodology and details of the datasets are presented in Section 3. The findings arising from this study are discussed in Section 4, and the main conclusions summarised in Section 5.

2. Background

Adopting linear random wave theory (LRWT), the water surface elevation correct to first order, $\eta^{(1)}(\mathbf{x},t)$, can be expressed as:

$$\eta^{(1)}(\mathbf{x},t) = \sum_{i=1}^{\infty} a_i \cos\left(\mathbf{k}_i\mathbf{x} - \omega_i t + \psi_i\right), \tag{2}$$

where $\mathbf{x} = (x, y)$ is the horizontal coordinate vector, i denotes an individual wave harmonic of amplitude a_i and initial phase ψ_i, and $\mathbf{k} = (k_x, k_y) = (k\cos\theta, k\sin\theta)$ is the wavenumber vector associated with the cyclic frequency, ω, and direction, θ, via the linear dispersion relation. Adopting this approach the water surface elevation represents a zero-mean, random Gaussian process (Ochi 1998). As such, Lindgren (1972), Boccotti (1983) and Tromans et al. (1991) used the asymptotic properties of Gaussian theory to derive the most probable shape of the largest waves. This approach is commonly referred to as the theory of Quasi-Determinism or QD-wave (Boccotti 2000). Alternatively, Tromans et al. (1991) re-labelled these events as “NewWaves” and this notation has been adopted in some design codes (ISO:19901-1 and API 2MET). Irrespective of the name adopted, the average shape of the largest waves arising in a (stationary) sea-state was shown to be proportional to its normalised autocorrelation function, $r(\tau)$. Removing the spatial dependence from Equation (2), the temporal QD-wave profile at a single location is given by:

$$\eta_{\mathrm{QD}} = Ar(\tau) = A\frac{\int_0^{\infty} S_{\eta\eta}(\omega)\cos(\omega\tau)\mathrm{d}\omega}{\int_0^{\infty} S_{\eta\eta}(\omega)\mathrm{d}\omega}, \tag{3}$$

where $S_{\eta\eta}(\omega)$ is the energy density function, τ is the time-lag (measured from the maximum of $r(\tau)$) and A a scaling factor that can be adjusted to approximate the maximum crest elevation, η_{max}. Theoretically, this approximation is valid for $\eta_c/\sigma_\eta \to \infty$, where η_c is the crest height and σ_η the standard deviation of the surface elevation time-series. However, as discussed in Section 4, the practical application of this model requires the definition of a large but finite value for this ratio.

While the QD-wave profile provides a good approximation for linear sea-states (Boccotti et al. 1993; Phillips et al. 1993a,b), real seas are nonlinear, particularly those of interest in design. As a result, the largest waves arising in these seas will inevitably exhibit some level of nonlinear behaviour (Guedes Soares and Pascoal 2005). At a second-order of wave steepness, the free surface elevation is given by the sum of the linear part [Eq.(2)] and the second-order bound contributions. The latter are further divided into the frequency-difference terms ($\eta^{(2-)}$) and the frequency-sum terms ($\eta^{(2+)}$), as described by Longuet-Higgins and Stewart (1960) and Sharma and Dean (1981). These are given by:

$$\eta^{(2-)}(\mathbf{x},t) = \sum_{i=1}^{\infty}\sum_{j=1}^{\infty} M^{ij-}\cos(\Psi_i - \Psi_j) \tag{4}$$

$$\eta^{(2+)}(\mathbf{x},t) = \sum_{i=1}^{\infty}\sum_{j=1}^{\infty} M^{ij+}\cos(\Psi_i + \Psi_j), \tag{5}$$

where the interaction kernels M^{ij-} and M^{ij+} are given in the Appendix and $\Psi = (\mathbf{kx} - \omega t + \psi)$ for each $(i,\, j)$ wave harmonic. Considering these contributions, the frequency-difference terms represent slowly varying terms (or group terms), while the frequency-sum terms are high-frequency oscillations. Taken together, the total surface elevation according to second-order random wave theory (SORWT) is: $\eta^{(2)} = \eta^{(1)} + \eta^{(2-)} + \eta^{(2+)}$. To capture the effects arising at a second-order of wave steepness, Jensen (1996, 2005); Fedele and Arena (2005); Tayfun (2006a) and Tayfun and Fedele (2007) have derived analytical corrections to the linear QD-wave profile. These second-order corrections have been shown to provide a better approximation to the average profile of the largest waves recorded in field data; evidence provided by Tayfun and Fedele (2007). For this reason, both the linear and second-order QD-wave profiles are examined in the present study; the latter being obtained explicitly from SORWT (Arena 2005).

An alternative method to account for nonlinearities has been applied by Johannessen and Swan (2003); Walker et al. (2004); Taylor and Williams (2004); Santo et al. (2013) and Whittaker et al. (2016) amongst others. In this case, the average profiles of waves with the largest crest heights and deepest toughs are employed to decompose the nonlinear contributions. A Stokes-type expansion is then used to obtain the nonlinear wave profile. This method has been shown to be quite versatile in terms of the order of nonlinearity that can be included; Walker et al. (2004) incorporating effects up to a fifth-order of wave steepness.

One particular category of large ocean waves relates to so-called *rogue* waves. These represent wave events that are significantly larger than the surrounding wave field in a given sea-state. The most common definition is that proposed by Haver and Andersen (2000) in which $\eta_{\max} > 1.25H_s$ or $H_{\max} > 2H_s$, where H_s is the significant wave height and the ratios are based upon a 20-minute record. Such events are commonly said to be responsible for a number of marine accidents (Kharif and Pelinovsky 2003). Increasing evidence in the literature suggest that a physical mechanism that leads to the formation of these wave events arises through the spatio-temporal focusing of individual wave harmonics (Christou and Ewans 2014; Cavaleri et al. 2016; Benetazzo et al. 2017); the linear focusing under-pinning the QD-wave being enhanced by higher-order nonlinearities.

While some studies suggest that effects higher than second-order are insignificant (Fedele et al. 2016), others have shown evidence of their importance in experimental and field measurements (Latheef and Swan (2013), Gibson et al. (2014) and Karmpadakis et al. (2019)). It is clear that in a linear sense a QD-wave profile and a focused wave are identical; the input spectrum for the latter being the Fourier transform of Equation (3). Nonlinear effects can therefore be investigated by generating focused waves either experimentally (Baldock and Swan 1996; Johannessen and Swan 2001) or numerically (Johannessen and Swan 2003; Bateman et al. 2012; Adcock and Taylor 2016). The aforementioned studies have provided significant insights into the nonlinear physics that drive the formation of large wave events. Two characteristic changes relate to increased crest height elevations above second-order theory and front-back asymmetry of the largest wave event at the time of focusing; the latter being induced by its movement towards the front of the wave group. Taking into account that neither of these nonlinear changes is captured by the analytical QD-theories, it is worth considering whether they are relevant to the definition of the average shape of the largest waves in random seas.

While many of the aforementioned studies investigate the shape of the largest waves in deep-water conditions, fewer studies have considered shallower water conditions (Whittaker et al. 2016). Considering the significance of large waves in finite water depths (Nikolkina and Didenkulova 2011; Karmpadakis 2019), the potential mechanisms of nonlinear amplifications (Slunyaev et al. 2002; Katsardi et al. 2013; Fernandez et al. 2014) and the effects of wave breaking (Katsardi and Swan 2011; Karmpadakis et al. 2020), this study concentrates on finite water depth conditions.

3. Data sources and methods of analysis

Three complementary sources of data have been used in the present paper. These include the analysis of surface elevation measurements recorded at the field, laboratory observations and numerical simulations. In each case the average shapes of the largest waves are compared to theory, and the effects of nonlinearity and wave breaking investigated.

a. Field data

The field data used within this study were recorded using wave radars mounted on the side of fixed offshore platforms. These were part of an extensive field data analysis project (the LoWiSh Joint Industry Project) including measurements from 10 different locations in the central and southern North Sea (Karmpadakis et al. 2020). In the present study, data from the shallowest and deepest locations are considered; the two platforms being located in water depths of 7.7 m (close to the Dutch coast) and 45 m (in the Danish sector) respectively. In both cases the free surface was recorded using Saab wave radars with high sampling rates ($4\,\mathrm{Hz} \leq f_s \leq 5.12\,\mathrm{Hz}$); the accuracy estimated to be ± 6 mm. Indeed, these measurements are in accordance with the highest standards in platform-based observations; a recent review of the operational characteristics of the instrument type being provided by Ewans et al. (2014). More importantly, the use of recordings from fixed instruments avoids potential issues that have been observed in the analysis of large waves using wave buoys. These include the linearisation of the measured waves and the movement around the largest, three-dimensional, wave crests (James 1986; Magnusson et al. 1999; Dysthe et al. 2008). Moreover, the adopted sampling rate guarantees that the nonlinear characteristics of the largest waves can be captured with sufficient accuracy. In this respect, low sampling rates have been shown to underestimate the largest crest elevations (Tayfun 1993; Stansell et al. 2002).

In seeking to obtain a high quality database, the raw surface elevation records were processed according to the strict quality control (QC) procedures outlined by Christou and Ewans (2014). In effect, this involves the application of a series of flags to identify potential sources of error; the latter including instrument lock-ins, sensor drifts and unrealistic spikes in the surface elevation records. When erroneous measurements were identified, the full 20-minute record was abandoned. All remaining (un-flagged) records were then processed using standard spectral and zero-crossing analysis methodologies. It is also important to note that any tidal fluctuations or storm surges were removed prior to the commencement of the analysis. Having completed the analysis of each 20-minute record, appropriate met-ocean parameters, such as the significant wave height (H_s) and peak period (T_p), were used to bin the the resulting sea-states into small groups with similar characteristics. The largest waves recorded in the sea-states within each of these data bins were then extracted and are presented in the analysis that follows.

b. Experimental data

In generating the laboratory wave data, a large number of random sea-states were simulated in the directional wave basin at Imperial College London. This wave basin has plan dimensions of 10 m x 20 m and a movable horizontal bed; the water depth in the present tests being set to $d = 0.5$ m. The basin is equipped with 56 individually controlled, bottom-hinged wave paddles positioned along the 20 m length. The wavemakers operate on the basis of a theoretical transfer function with active, force-feedback, wave absorption (Spinneken and Swan 2012). The combination of the active absorption system and a perforated parabolic beach on the opposite side of the wavemakers ensures that the maximum reflection coefficients were less than 5%. Moreover, there is no build-up of reflected wave energy within the wave basin during a long random generation (Masterton and Swan 2008).

The time-histories of water surface elevation, $\eta(t)$, were recorded using 32 resistance-type wave gauges. These gauges comprise of two thin steel wires (of diameter 1.5 mm) spaced 10 mm apart and were calibrated daily to maintain an accuracy of ± 0.5 mm. The sampling rate was sufficiently high ($f_s = 128$ Hz) to ensure that $\eta(t)$ was measured accurately and no post-processing or filtering was required. Importantly, Haley (2016) has demonstrated that this configuration can accurately record the surface elevation of both very steep and breaking waves. This was confirmed by comparing the output of these wave gauges with high-speed video imaging. The layout of wave gauges for the experiments presented herein consists of a 5 x 5 array in the centre of the wave basin, with 7 additional wave gauges placed along the centreline of the wave basin. Full details of this layout are given in Karmpadakis et al. (2019). Importantly, the minimum distance between the upstream wave gauge and the wavemakers ($l = 2.3\,\mathrm{m}$) was larger than $3d$. This ensures that there were no evanescent wave modes present in the measured data. The operational characteristics of this facility yield results that are spatially homogeneous in the working area of basin (Latheef and Swan 2013). As such, unless otherwise stated, the results presented correspond to measurements at the central wave gauge; the latter being representative of the full wave gauge array.

All the experiments involve random, directionally spread, sea-states. To ensure that the sea-states under consideration correspond to realistic conditions in the field, they were defined on the basis of the JONSWAP spectrum (Hasselmann et al. 1973); the spectral density function, $S_{\eta\eta}$, for each case defined by:

$$S_{\eta\eta}(\omega) = \frac{\alpha g^2}{\omega^5} \exp\left(\frac{-\beta \omega_p^4}{\omega^4}\right) \gamma^{\exp\left[-\frac{(\omega-\omega_p)^2}{2\sigma^2\omega_p^2}\right]}, \tag{6}$$

where ω is the circular wave frequency ($\omega = 2\pi/T$), T the corresponding wave period, ω_p circular wave frequency at the spectral peak, $\beta = 1.25$, $\sigma = 0.07$ for $\omega \leq \omega_p$ and $\sigma = 0.09$ for $\omega > \omega_p$. To simulate sea-states with finite frequency bandwidth, the peak enhancement factor, γ, was set to 2.5 for all test cases. The Phillips parameter, α, was adjusted in each test case so that the target H_s could be obtained for a given spectral peak period, T_p. Although the JONSWAP spectrum does not represent the present state-of-the-art when modelling real seas (see, for example, Lenain and Melville (2017)), it is widely applied in engineering practice and has been adopted as the basis for many earlier studies. Moreover, it provides a reasonable description of the field data employed in the present study. To generate directionally spread sea-states, a wrapped-normal directional spreading function (DSF) was applied to the uni-directional spectra defined in Equation (6). The functional form of the DSF is given by:

$$D(\omega,\theta) = \frac{A}{\sigma_\theta}\exp\left(-\frac{\theta^2}{2\sigma_\theta^2}\right), \tag{7}$$

where θ is the angle of propagation, measured relative to the x-axis, σ_θ is the standard deviation of the frequency independent directional spreading and A is a normalising factor such that $\int_0^{2\pi} D(\omega,\theta)d\theta = 1$. The directional spectrum is thus given by: $F(\omega,\theta) = S_{\eta\eta}(\omega)D(\omega,\theta)$. Further details concerning the effective generation of directionally spread seas are given in Latheef et al. (2017). Given the nature of the input conditions, the target sea-states can be uniquely defined by 3 parameters: (H_s, T_p, σ_θ). In relating the experimental test cases to field measurements, scaling based on Froude number similarity has been applied. Specifically, a length-scale of $l_s = 1:100$ and a corresponding time-scale of $t_s = \sqrt{l_s} = 1:10$ have been adopted throughout these tests.

The analysis in the present paper focuses on test cases with $k_pd = 1.22$ ($T_p = 1.4\,\text{s}$) and $\sigma_\theta = 10^\circ$; a variety of sea-state steepnesses being examined. These cases correspond to a wide variety of realistic sea-state conditions in which a detailed investigation of the effects of nonlinearity and wave breaking is conducted. In validating the results obtained in these conditions, additional sea-states were also considered. In total, these involve 3 different effective water depths, $k_pd = 1.53$, 1.22 and 1.02, each with directional spreads of $\sigma_\theta = 0^\circ$, 10° and 20° and a range of sea-state steepnesses (S_p). A summary of the relevant experimental test cases is provided in Table 1.

The selection of the test cases presented in Table 1 was primarily driven by the need to investigate the changes induced by increasing sea-state steepness in finite water depths. In this respect, the sea-state steepness, S_p, is defined as:

$$S_p = \frac{2\pi H_s}{g T_p^2}, \tag{8}$$

where $g = 9.81\,\mathrm{ms}^{-2}$ is the gravitational acceleration. The significant wave height, H_s, in each test case was selected to provide an incremental increase in S_p, such that $\Delta S_p = 0.01$. Taken together, the sea-states presented herein vary from near-linear ($S_p = 0.01$) to extremely steep ($S_p = 0.06$); the latter being characterised by extensive wave breaking.

For each of these test cases, 20 random simulations or seeds were undertaken; the duration of a single simulation being 1024 s. Given the adopted scaling, each simulation (approximately) corresponds to a 3-hour sea-state at field-scale. Furthermore, the target spectrum used as input to the wavemakers comprised of frequency components lying in the range $0.4\,\mathrm{Hz} < f < 2.5\,\mathrm{Hz}$ and had a resolution of $\Delta f = 1/1024\,\mathrm{Hz}$. This yields a set of 2145 individual wave components that define each random seed. The amplitude of each wave component was defined by the target JONSWAP spectrum without being further randomised. This means that the (one-dimensional) energy spectra for each seed within the same test case are identical. The initial phase (ψ) of each individual wave component was chosen randomly from a uniform distribution lying in the range $[0, 2\pi)$. Additionally, each individual wave component was assigned a direction of propagation (θ). These varied between $-45^\circ \leq \theta \leq 45^\circ$ and were randomly sampled from the target DSF defined in Equation (7). It should be noted that the adoption of this method leads to the generation of individual frequency components propagating in a single direction and is effectively a modification of the Single Summation Method (Miles and Funke 1989), often called the Random Directional Method (RDM). Latheef et al. (2017) have shown that the RDM method has significant advantages when it comes to generating ergodic, directionally spread sea-states.

A subtle but very important point regarding this experimental investigation concerns the treatment of the initial phases and directions of propagation between the seeds of different test cases.

Specifically, a set of random phases and directions were defined for each seed in the lowest steepness case (for example, case B1-10 with $S_p = 0.01$ and $\sigma_\theta = 10°$- see Table 1). For the cases with larger S_p (but the same T_p and σ_θ), the sets of phases and directions were kept unchanged. As a result, the amplitude of the individual wave components is the only variable that changes between the same seeds in sea-states of different steepnesses. This methodology leads to a collection of 20 random simulations or seeds for each sea-state. However, each single seed has the same "random" characteristics in all test cases with the same effective water depth and directional spreading. In other words, the Inverse Fourier Transform of the input directional spectra of the same seed in different sea-states provides time-histories that are exactly aligned; the only difference between them being the scale of $\eta(t)$. This alignment is clearly shown on Figure 2 which presents the same 5-second segment of the surface elevation, $\eta(t)$, time-histories from seed 11 in cases A1-10, A2-10 and A3-10; their steepnesses being $S_p = 0.01, 0.02$ and 0.03 respectively. The main advantage of this method lies in the ability to perform direct comparisons between individual wave events within random, directionally spread sea-states with increasing steepness. As such, its application is critical in identifying the effects driven by increases in nonlinearity; the latter arising at second-order of wave steepness and above.

c. Numerical Simulations

To take full advantage of the experimental method described above, numerical simulations were also performed using second-order random wave theory (SORWT) based upon Sharma and Dean (1981). These were generated using the same input conditions and output locations as in the experiments. This allows the direct superposition of experimental and numerical results. Figure 3 presents examples of time-histories of the water surface elevation, $\eta(t)$, recorded on the centreline of the wave basin with direct comparisons to the predictions of SORWT. Figure 3(a) concerns a near-linear sea-state ($S_p = 0.01$, $k_p d = 1.02$, $\sigma_\theta = 10°$) and shows very good agreement between the experimental and numerical results. This agreement indicates that second-order random wave theory is sufficient to describe the wave field and acts to validate the accuracy of the adopted wave generation. More importantly, the agreement in both space and time indicates that the wave field is not contaminated by any spurious waves or significant reflections; further validation being provided in Karmpadakis et al. (2019). Figure 3(b) concerns the same time segment, but corresponds to a more nonlinear sea-state ($S_p = 0.02$). Overall, the experimental and numerical results show good agreement, but some differences arise during the formation of the largest wave event. For example, the wave recorded at the last wave gauge, around $t \approx 964\,\mathrm{s}$, is larger than its second-order counterpart. Karmpadakis et al. (2019) have attributed this increase to the effects of higher-order nonlinear interactions and discussed its implications for the short-term distribution of crest heights (see Figure 1). In figure 3(c), the sea-state steepness has been further increased to $S_p = 0.03$. In this case, the wave event identified above is shown to be smaller than the SORWT prediction at all locations and arrives at the last wave gauge earlier. Considering that the surrounding wave field is described reasonably well by the numerical simulations, this decrease in the surface elevation indicates that the wave recorded in the experiment has broken. Clearly, this is not something that can be captured using second-order random wave theory.

Following a similar approach, Figure 4 presents results arising in sea-states with increasing steepness recorded at the central wave gauge. Figure 4(a) concerns time segments for sea-states with $S_p = 0.01$, $S_p = 0.02$ and $S_p = 0.03$; the experimental data again being compared to SORWT. In the less steep cases, the numerical results provide an accurate description of the wave field. However, discrepancies are apparent in the steepest case ($S_p = 0.03$). These are demonstrated in two ways. First, the crest height of the largest wave event in the experiment is larger than its SORWT counterpart. Second, the relative elevation of the wave troughs adjacent to the largest experimental wave crest is reduced compared to the second-order simulation. In explaining these changes, the effects of higher-order nonlinear interactions, arising at third-order and above, need to be considered. At a third-order of approximation, these interactions consist of both bound and resonant (or near-resonant) terms. The former contribute to the total surface elevation, but their magnitude becomes progressively smaller at higher-orders of nonlinearity. In contrast, resonant interactions act to modify the free wave spectrum and induce changes in the amplitude and phasing of the individual wave harmonics. As such, their contribution is to increase the total crest height elevation and change the shape of (at least) the largest wave event presented in this figure. In Figure 4(b), a near-linear sea-state ($S_p = 0.01$) is compared with a nonlinear ($S_p = 0.03$) and a highly nonlinear sea-state ($S_p = 0.06$). While similar conclusions can be drawn for the first two steepnesses, it is clear that the surface elevations for $S_p = 0.06$ show marked differences. The height of the largest wave crest in the experiment is smaller than the corresponding second-order crest height; the same wave having a larger crest when comparisons relate to a sea-state with $S_p = 0.03$. The reduced crest heights recorded in the steepest sea-states provide direct evidence of the dissipative effect of wave breaking.

Taken together, the methodology described above is used to provide temporal wave profiles from random experimental simulations that are influenced solely by the sea-state steepness; the alignment of the corresponding waves being clearly defined. By comparing these results with the predictions of second-order random wave theory, the effects of nonlinearity and wave breaking can be explicitly identified.

4. Discussion of results

While the study of individual wave events, such as those presented in Section 3, is very informative, the focus of the present study lies in the characteristics of the largest waves. This is addressed by investigating their average shape (in time) in both field and laboratory measurements. To obtain these average wave shapes, a common approach is to extract a short time segment of the surface elevation, $\eta(t)$, around the largest crest heights. The (shortened) time-histories are then shifted in time such that the maximum crest elevation occurs at $t = 0\,\mathrm{s}$ and averaged. While this approach has been widely applied in the literature (Phillips et al. 1993b; Jonathan and Taylor 1997; Guedes Soares and Pascoal 2005; Whittaker et al. 2016), the exact number of waves being averaged varies between studies. In many field related studies, the 20 largest waves arising in sea-states of 30 minutes duration are used, while in others some fraction of η_c/σ_η is preferred. As indicated in Section 2, the theoretical limit of $\eta_c/\sigma_\eta \to \infty$ cannot be applied in practice.

In an effort to select an appropriate (and consistent) number of individual waves to include in the averaging process, a large number of numerical simulations were performed using linear random wave theory (adopting the methodology outlined in Section 3). To this end, 50 random seeds, each of 3-hour duration (at field-scale), were used to extract the largest waves corresponding to different percentiles; the latter including the largest [0.1%, 0.2%, 0.5%, 1%, 2% and 5%] waves in each seed. The inclusion of a larger number of waves inevitably leads to a downscaling of the resulting profile, $\overline{\eta(t)}$, since smaller waves are included in the averaging process. In contrast, the inclusion of only a small number of waves within the averaging process increases the statistical variability and (consequently) introduces deviations from the symmetric profile of a QD-solution.

In seeking to define the optimal number of waves to be included within the averaging process, two metrics are defined. First, the ratio between the maximum of the average wave profile at each percentile and the maximum corresponding to the smallest percentile, $\bar{\eta}_{max}/\bar{\eta}_{max}^{0.1\%}$ is considered. The second metric is the root-mean-square (RMS) error, $\varepsilon_{\mathrm{rms}}$, between the average wave profiles and the scaled QD-wave profile (η_{QD}); the scaling factor based upon the maximum crest height,

$\eta_{\max}$, in each case. This second metric is defined by:

$$\varepsilon_{\text{rms}} = \frac{1}{N}\sqrt{\sum_{i=1}^{N}(\bar{\eta}_i - \eta_{\text{QD},i})^2}, \tag{9}$$

where i corresponds to each observation and N is the total number of time steps in the time-histories, $t \in [-2T_p, 2T_p]$. Figure 5 presents the values of these metrics for each percentile under consideration; the two vertical axes having different scales. These show that the average maximum crest height decreases monotonically, with the inclusion of more (smaller) waves, while the minimum rms error (ε_{rms}) is observed for the 1% percentile. Specifically, ε_{rms} reduces towards the 1% percentile, as more waves are included, but then increases for larger percentiles. This indicates that the smaller waves added for increased percentiles violate the asymptotic assumptions of the QD-wave profile. In such cases an alternative representation should be sought (Lindgren 1970, 1972). Using this guidance, the 1% of the largest waves is used when calculating the average wave shapes for the remainder of the present paper. This percentile corresponds to a ratio $\eta_c/\sigma_\eta \approx 3$, which has been proposed by some earlier studies (Phillips et al. 1993a) and is justified theoretically by Cartwright and Longuet-Higgins (1956). It is also important to note that similar results regarding the statistical variability arise if the Lindgren variance is used as an alternative (Lindgren 1972); the latter quantifying the statistical variability when moving away from the largest crest height. However, the approach adopted herein relates directly to the experimental method and provides a simpler alternative.

Having selected the optimal number of waves to consider, the average profile of the largest waves can be readily calculated. While field observations generally provide the most accurate representation of realistic conditions, it is seldom possible to record sufficiently long time-series in severe sea-states. In this respect, laboratory experiments can be used to address the lack of data in the steepest sea-states. However, the experimental generation of large waves in shallow water is extremely difficult due to unrepresentative energy losses by bed friction and the inherent limitations of wavemaking theory; the latter associated with the increased importance of the second-order difference terms as d reduces. To address these issues, the experimental and field datasets are used in a complementary manner to provide comparisons to the QD-predictions.

These comparisons are shown on Figure 6. In all cases the average wave profiles have been normalised by their maximum elevation ($\eta_{\max}$). As such, the (vertical) deviations between the theoretical and measured wave profiles appear as differences in the depth of the adjacent wave troughs. In two examples (Figures 6(a) and 6(c)), the light gray lines correspond to the individual measured wave profiles used within the averaging process; the first relating to laboratory data and the second to field data. Comparisons between these profiles show that the observed variability is similar in the two datasets. Figures 6(a) and 6(b) present comparisons between experimental results and the QD-wave profiles for $k_p d = 1.22$ and $\sigma_\theta = 10°$. In the moderate sea-state ($S_p = 0.01$) presented in sub-plot (a), the linear and second-order corrected QD-wave profiles are closely aligned, given the limited nonlinearity, and agree very well with the measured data. In contrast, sub-plot (b) considers the nonlinear sea-state ($S_p = 0.04$) and shows that the measured profile deviates markedly from the theoretical predictions. These deviations are apparent both in the adjacent wave troughs and the front slope ($\partial\eta/\partial t$) of the largest wave; the measured data exhibiting both a steeper gradient and a narrower crest. These observations indicate nonlinear contributions that are not captured by the QD models. However, it is important to note that the second-order correction to the QD-wave profile provides notably better predictions than its linear counterpart.

Following a similar approach the average wave profiles recorded in the field are also compared to theory. In defining the sea-states to consider at each of the two locations, the data-binning methodology (Section 3) was adopted. To achieve the largest possible homogeneity, the selection was based upon a maximum variation of $\pm 5\%$ in the sea-state parameters (H_s, T_p and T_1); where T_1

defines the mean wave period. Figures 6(c) and 6(d) relate to measurements from the deepest location ($d = 45\,\mathrm{m}$), while Figure 6(e) relates to the shallowest location ($d = 7.7\,\mathrm{m}$). Interestingly, the sea-states in sub-plots (c) and (d) are characterised by a similar effective water depth ($k_p d \approx 1.4$) but different steepnesses $S_p = [0.018, 0.027]$. In the former case, it can be seen that the linear QD-wave profile does not agree well with the measurements. In contrast, the second-order corrected QD-wave profile closely follows the measured average profile. Similar conclusions arise when the steeper case is considered (sub-plot (d)). However, the improvement provided by the second-order correction is not sufficient to approximate the measured profile. Considering that these correspond to steeper sea-states the explanation lies in the effects of nonlinearity arising above second-order. In addition, wave breaking will also be present; the extent to which it influences the results being examined in what follows. While these results are in agreement with the findings of Guedes Soares and Pascoal (2005), most studies in the literature (Section 2) do not identify such deviations; the absence of reliable data in sufficiently steep sea-states being the most probable explanation. More importantly, the results presented in sub-plot (e) exhibit clear nonlinear behaviour with steep front and back wave slopes ($\partial\eta/\partial t$), a sharp wave crest and flat wave troughs; all of them being indicative of the small effective water depth ($k_p d \approx 0.75$). As such, the linear QD-wave profile presents widely different predictions; the second-order correction being outside its range of validity (Tayfun 2006b). This last example is indicative of the vast majority of the results obtained in this water depth; irrespective of sea-state steepness. This raises significant concerns regarding the applicability of the QD-wave approach in very shallow effective water depths.

With the laboratory data used to extrapolate findings into steeper sea-states that have either not been encountered in the field or for which insufficient data is available, it is crucial to verify that the two independent data sources provide the same results in those cases where there is an overlap between the two. Figure 7 presents an example of a direct comparison between the average profiles of the largest waves recorded in the laboratory and the field for similar sea-states. To achieve this, a nearest neighbour algorithm was employed to identify the sea-states from the deepest field location ($d = 45\,\mathrm{m}$) that matched experimental cases in terms of the nondimensional parameters (S_p, $k_p d$). A requirement for $T_1/T_p \approx 0.82$ (DNV 2010) was also enforced to obtain sea-states with peak enhancement factors similar to the experiments ($\gamma = 2.5$). The observed agreement indicates that the experimental measurements can accurately describe the conditions encountered in the field. More importantly, the fact that this agreement is observed in a sea-state with $S_p = 0.03$ provides additional confidence because noteworthy nonlinear effects have been observed in the crest height statistics for similar sea-state conditions (Karmpadakis et al. 2019).

To elaborate on this, the average wave shapes arising in experimentally generated sea-states with increasing steepness are further investigated on Figure 8. The conditions correspond to $k_p d = 1.22$ and $\sigma_\theta = 10^\circ$ and have been normalised with respect to the standard deviation of the free surface (σ_η) and the mean period (T_1). Sub-plot (a) presents results corresponding to $S_p = 0.01, 0.02,$ and 0.03, while sub-plot (b) relates to sea-states with $S_p = 0.04, 0.05,$ and 0.06. It is clear that in the former case, an increase in sea-state steepness leads to more nonlinear average wave profiles; the nonlinearities being manifested as increases in the crest elevation, steepening of the wave slopes ($\partial\eta/\partial t$) and flattening of the wave troughs. In contrast, in the steepest sea-states (sub-plot (b)) the reverse trend is observed; particularly considering the maximum crest height. Indeed, increases in the sea-state steepness lead to a reduction in the maxima of the average profiles. Importantly, the average profiles in sub-plot (a) show little or no evidence of horizontal asymmetry, while some minor asymmetries are observed in sub-plot (b); the wave troughs preceding the largest crest being marginally shallower than that which follows.

If these results are examined in isolation, the aforementioned observations could largely be attributed to bound nonlinear interactions and the limited influence of wave breaking; the former used to justify the nonlinear changes observed in Figure 8(a) and the latter the energy dissipation in Figure 8(b). As a consequence, an observed agreement with a weakly nonlinear QD-profile would not seem unreasonable, as suggested in the literature (Section 2). However, any interpretation that nonlinear resonant (or near-resonant) effects are not significant is misleading. This is because the population of the largest measured waves will likely include both breaking and non-breaking waves; their characteristics potentially averaging out important nonlinear changes. To illustrate this, the distributions of crest heights (η_c) arising in all sea-states ($S_p = 0.01 - 0.06$) are considered on Figure 9. For each sea-state, these are based upon a zero-crossing analysis of the time-histories of each individual seed. Given that the crest heights in each seed (of the same sea-state) represent random samples of the same population, they can be combined into a single larger sample, ranked in descending order and plotted against their probability of exceedance (Q). In this way, results with much lower probabilities of exceedance, lying at the tail of the distribution, can be examined. Subsequently, the 5 largest crest heights arising in the second-order simulation for $S_p = 0.01$ are identified and correlated to their corresponding wave events in the laboratory measurements. As the steepness of the sea-states is scaled-up these wave events are tracked taking advantage of the (time) alignment of the coupled numerical and experimental datasets (Section 3). These are then superimposed on Figure 9; their corresponding probability of exceedance (Q) being calculated on the basis of their rank at each sea-state.

In examining these results, it is clear that the waves that exhibit the largest crest height in the near-linear case $S_p = 0.01$ do not maintain their rank (as the largest) in the steeper cases. In fact, they are redistributed towards larger probabilities of exceedance from $S_p = 0.02$ onwards. The range of probabilities which they occupy is also clearly broadening as the sea-state steepness is increased. In the steepest case their probabilities range from 10^{-1} to $3 \cdot 10^{-3}$ and only one is still ranked in the largest 5 waves in the 3 sea-states with $S_p > 0.03$. It is worth keeping in mind that if the corresponding statistics were generated on the basis of SORWT results, these waves would maintain their rank; since no energy transfers or wave breaking are incorporated. For the experimental results, the migration towards larger probabilities of exceedance is justified by the occurrence of wave breaking and the associated wave energy dissipation. This implies that eventually the largest waves in a linear (or second-order) simulation are more susceptible to wave breaking and will not remain the largest as the steepness of the sea-state is increased. As a result, their place in the ordered set of crest heights will be occupied by a different wave which will correspond to a smaller linear (or second-order) equivalent. This result has far-reaching implications with respect to the interpretation of crest height (or wave height) distributions. Generally, it is well-established that the occurrence wave breaking leads to crest height reductions and, consequently, waves moving towards larger probabilities of exceedance. However, thus far this movement was considered to be relatively small; the largest waves considered to remain in the tail of the distribution despite the reductions, as discussed by Battjes and Groenendijk (2000). In view of the results presented herein it is clear that this is not the case; the breaking waves being characterised by probabilities that are typically associated to small non-breaking waves. In this respect, the novelty of the adopted approach of coupling numerics and experiments, as well as sea-states with different steepness, becomes apparent and is shown to be very insightful.

With the aim to further clarify these points, this approach is extended to define separate populations of breaking and non-breaking waves. More specifically, the total population of the normalised crest heights in the SORWT simulations ($\eta_c^{(2)}/H_s$) is partitioned into bins of width $\Delta\eta_c^{(2)}/H_s = 0.1$ for $\eta_c^{(2)}/H_s > 0.5$. The corresponding normalised crest heights from the laboratory simulations are identified in the same manner as above and the ratio ($r = \eta_c/\eta_c^{(2)}$) between the two is calculated on a wave by wave basis. As such, $r > 1$ means that the measured crest height is larger than SORWT, while the opposite is true for $r < 1$. This ratio is then used to detect whether an individual (zero-crossing) wave is being amplified (by nonlinearity) or dissipated (by breaking). To avoid the influence of small fluctuations in the measured water surface a "buffer" of 5% in the calculated values for r is imposed. Therefore, a wave is labelled as breaking if $r < 0.95$, and amplified if $r > 1.05$; a sensitivity analysis on the width of the "buffer" zone showing that no qualitative changes arise when different bands are considered. In this context, the term "breaking" refers to waves that are exhibiting some level of dissipation with respect to the predictions of SORWT. In this sense, these include waves that have already broken when they arrive at the measuring location. Therefore, this criterion is different to the classic geometric, kinematic and dynamic criteria (Babanin 2011; Perlin et al. 2013) which identify incipient breaking and should not be interpreted as such.

The aforementioned definitions are applied to the partitioned data to derive the conditional probabilities of amplification (P_a) and breaking (P_b) as the ratio between the number of waves in each population over the total number of waves contained in each bin. These probabilities are shown in Figure 10 for all the sea-states with $k_p d = 1.22$ and $\sigma_\theta = 10°$. Considering the probability of amplification in sub-plot (a), it can be seen that as $\eta_c^{(2)}/H_s$ increases the probability of a (second-order) wave being amplified reduces across all sea-state steepnesses. Moreover, as the sea-state steepness increases, the probability of amplification for the smallest (second-order) waves is also increased, while it is rapidly reduced for the largest waves. Considering the probability of breaking in sub-plot (b), the opposite trends are observed; the largest (second-order) waves are progressively more likely to break as $\eta_c^{(2)}/H_s$ and S_p increase. Wave breaking is observed even in the most moderate sea-states with small S_p. In undertaking this analysis, it is worth noting that data bins with fewer than 5 points have been excluded in the calculation of both probabilities. When the two plots are examined together, it becomes clear that the reason why the largest (second-order) waves are not further amplified is because they are breaking; for example $\eta_c^{(2)}/H_s = 0.8$ for $S_p = 0.06$.

These results justify the observations discussed earlier with respect to tracking the relative rank of crest heights in the total population of waves (Figure 9). This has clear implications when it comes to selecting individual wave events for a wide range of design applications or the calculation of extremal statistics; the main conclusion being that the largest wave in a fully nonlinear sense will not necessarily stem from a wave that is found in the tail of a linear or second-order crest height distribution. In contrast, the largest waves in the steepest sea-states may well correspond to much smaller linear or second-order waves.

In effect, the results presented in Figure 10 clearly show that across a wide range of $\eta_c^{(2)}/H_s$ breaking and non-breaking waves will be present in sea-states of varying steepness. The question that immediately arises is whether the average shapes of the largest waves in these two populations have the same characteristics. To address this, the same approach of wave classification is employed to investigate the largest 1% of waves; the latter referring to the experimentally measured data instead of SORWT simulations. After classifying each wave as breaking and non-breaking the wave profiles of each population are extracted from the experimental and numerical time-histories, time-shifted and averaged. Given that the waves included in the averaging process correspond to the same events in the numerical and experimental datasets, the comparisons of their average profiles are deterministic. As such there is significantly more information carried than simply comparing averages from uncorrelated samples. Such comparisons have not previously been presented in the literature.

First, the average profiles of the largest non-breaking waves are considered. Figure 11 presents comparisons between the corresponding linear, second-order and experimental wave profiles. Considering data with $k_p d = 1.22$ and $\sigma_\theta = 10^\circ$, sub-plots (a) and (b) show results for a very moderate ($S_p = 0.01$) and a steep ($S_p = 0.04$) sea-state respectively. In the former, the largest non-breaking waves agree well with the second-order results and are only marginally larger then the linear predictions. This confirms that the waves are weakly nonlinear; the dominant nonlinear effects arising at a second-order of wave steepness. In contrast, the comparison in the steeper sea-state shows two important effects. First, the maximum crest heights observed experimentally are larger than the second-order predictions. The magnitude of this difference is at least comparable to the difference between LRWT and SORWT suggesting that it cannot be justified solely by higher-order bound contributions; the magnitude of the latter being one order of magnitude smaller (Fedele et al. 2016). Considering the deterministic nature of these comparisons, this observation supports the importance of resonant and near-resonant interactions (Slunyaev et al. 2002; Fernandez et al. 2014) in these random records. This is further supported by the amplifications in the crest height statistics above the (second-order) Forristall (2000) model for the same data discussed by Karmpadakis et al. (2019). Second, when considering the depth of the adjacent wave troughs another important difference is observed. The following wave trough in the experimental measurements appears to be shallower than the corresponding SORWT and LRWT prediction. This indicates the aforementioned higher-order interactions act to change the shape of the waves in a way that bound-interactions can not. In drawing an analogy with the study of focused wave groups, similar increases in the following wave troughs have been reported by Johannessen and Swan (2003) amongst others. In that respect the nonlinearities are manifested as a movement of the largest wave event towards the front of the group leading to a trough asymmetry. Conversely, if the measured data are considered in isolation, it is obvious that their profile is not symmetric but has a front-back asymmetry; the following trough being deeper than the preceding. This trend is observed in all the sea-states ($S_p > 0.02$) in this water depth ($k_p d = 1.22$). In addition, two representative examples are included for a deeper ($k_p d = 1.53$) and shallower ($k_p d = 1.02$) sea-state, both with $S_p = 0.03$ in Figures 11(c) and (d). In examining these examples the same conclusions are reached regarding nonlinear changes in the wave crest and wave shape thereby extending these findings to a wider range of effective water depths.

The results presented in Figure 11 have addressed the average shape of the largest non-breaking waves. In performing the same analysis on the population of breaking waves, their average shapes can again be extracted. These are now compared to the average wave profiles from the non-breaking population to illustrate the differences between them. Figures 12(a)-(d) present these comparisons for sea-state steepnesses between $S_p = 0.03$ and $S_p = 0.06$ for $k_p d = 1.22$. In comparing the profiles of the breaking and non-breaking waves, two important observations arise. First, the broken waves are characterised by smaller maximum crest heights, a clear manifestation of energy dissipation. Second, the breaking wave profiles exhibit a horizontal asymmetry that is opposite to the asymmetry of the non-breaking waves; the observation being consistent across all steepnesses. This means that the wave troughs preceding the largest crest elevations are deeper than the following wave troughs for the largest broken waves. Noting that these results represent a breakdown of the average wave profiles shown on Figure 8, the lack of significant asymmetries observed in the latter can be justified. In effect, the two different types of asymmetries for breaking and non-breaking wave populations largely cancel out, leading to a more symmetric wave profile when all waves are considered (for the largest 1%). This does not, however, imply that a weakly nonlinear QD-wave profile is appropriate, rather that important effects have been cancelled out by addressing two very different wave populations.

To verify that the interpretation of asymmetry presented so far is indeed important, we examine the statistics of the geometry of the largest waves. In this way, the results arising from the analysis of average wave profiles can be generalised. To achieve this, an asymmetry parameter β is defined as:

$$\beta = \frac{\eta_{pt}}{\eta_{ft}}, \tag{10}$$

where η_{pt} and η_{ft} are the preceding and following trough depths respectively. As such, if $\beta < 1$ a profile is exhibiting the characteristic non-breaking asymmetry, while the opposite is true for $\beta > 1$. This metric is used to examine the individual wave profiles corresponding to the largest 1% of waves arising in each individual sea-state. More specifically, the asymmetry parameter is calculated separately for the total, breaking and non-breaking populations of waves. Figure 13 presents the values of β for all sea-state steepnesses in $k_p d = 1.22$; sub-plot (a) relating to $\sigma_\theta = 10°$ and sub-plot (b) to $\sigma_\theta = 20°$. In this respect, the findings of this analysis are extended towards sea-states with different directional spreading. Additionally, the 95% confidence intervals has been added on the results of the total wave population as an indication of the variability in the estimates of β. In interpreting the results on Figure 13 it is clear that in both cases the non-breaking wave population has $\beta < 1$, the breaking population has $\beta > 1$ and that the total population lies between the two fluctuating around $\beta = 1$. This is exactly the same behaviour as discussed with respect to the average wave shapes and provides a significant validation of the results presented earlier. Moreover, a secondary trend in the the values of the asymmetry parameter β for the total and non-breaking populations can be observed. This refers to a decreasing trend in β for increasing steepness towards a local minimum (for example $S_p = 0.04$ in sub-plot (a)) followed by an increasing trend for larger steepnesses. This is implies that the nonlinear effects have a larger influence for increasing steepness until a critical steepness is reached. Beyond this point the effects of wave breaking become progressively more important; the latter leading to some degree of saturation. While this secondary trend is less clear for $\sigma_\theta = 20°$ it certainly coincides with the observed nonlinear effects in the crest height statistics which obtain a maximum for $S_p = 0.04$ (Karmpadakis et al. 2019).

Interestingly, comparisons between Figures 14(a) and 14(b) also allow some comments to be drawn concerning the role of directionality. For the non-breaking wave population ($\beta < 1$) it is clear that the higher-order amplifications remain significant, but are perhaps rather smaller with increases in the directional spread. Furthermore, in the breaking wave population ($\beta > 1$) an increase in the directional spread leads to smaller β values suggesting that breaking is rather less important, particularly for lower S_p values. These effects are consistent with the crest height distributions reported in Latheef and Swan (2013), Latheef et al. (2017) and Karmpadakis et al. (2019), following the expected reduction in the individual wave steepness with increasing directionality.

Finally, using these results an answer is provided as to why some studies of field data report symmetric average wave profiles even in relatively severe sea-state conditions (Christou and Ewans 2014; Gemmrich and Thomson 2017), while others have recorded asymmetries (Myrhaug and Kjeldsen 1986; Guedes Soares et al. 2004). The extent to which either type of asymmetry can be identified critically depends on the competing effects of nonlinear amplifications and the dissipative effects of wave breaking. Clearly, the method adopted in the experimental part of this study cannot be applied to field measurements where coupled simulations cannot be generated. However, the asymmetry parameter β can be used to assess whether any statistically significant trends are apparent in the present field data. To achieve this, the normalised zero up-crossing and down-crossing wave heights arising in all available sea-states are sorted and their probability of exceedance (Q) calculated. Using the ratio of the (ordered) wave heights the asymmetry parameter is calculated and plotted against Q on Figure 14; data recorded in the two water depths being superimposed. Considering $d = 45\,\mathrm{m}$, it can be seen that β fluctuates consistently around 1 for the vast majority of the data with some increases observed for the largest wave heights located in the tail of the distribution. In contrast, for $d = 7.7\,\mathrm{m}$ the asymmetry parameter is consistently larger than 1 indicating a strong presence of wave breaking. In interpreting these findings, the behaviour of β for the deeper location indicates the presence of both breaking and non-breaking waves which effectively cancel out their effects. This is consistent with the expected behaviour in intermediate and deep water locations and explained above (Figure 10). In contrast, for the shallowest location the observed asymmetry implies that wave breaking is the dominating process. Indeed, a recent analysis of wave height statistics at this location (Karmpadakis et al. 2020) has shown that there is a very strong presence of breaking waves, primarily driven by depth limitations. Since the majority of the largest waves are breaking the observed values of $\beta > 1$ are consistent with the analysis presented herein. Clearly, this example relates to the general population trends at each field location and not to the characteristics of individual sea-states; the latter being a natural extension of the present work.

5. Concluding remarks

The present paper has investigated the characteristics of the largest waves arising in random, directionally spread sea-states in finite water depths. This has been achieved using field, experimental and numerical data. The average profiles of the largest waves for a wide range of sea-states have been compared to the theory of Quasi-Determinism (QD). Whilst this undoubtedly provides a marked improvement over the "equivalent" regular waves commonly adopted in engineering design, it is not without its limitations. Specifically, comparisons to linear QD-wave profiles show good agreement for near-linear sea-states. With an increase in the sea-state steepness, the second-order corrected QD-wave profile incorporates some of the nonlinearity of the wave profile and provides a better approximation. However, very steep sea-states or sea-states in shallow water show significant departures from the theoretical predictions.

When considering the total population of the largest 1% of waves in sea-states with varying steepness, it was found that their average profile was either (horizontally) symmetric or characterised by very small asymmetries between the wave troughs adjacent to the largest crest. This is inconsistent with the observations of fully nonlinear focused wave groups that develop strong asymmetries due to the nonlinear physics arising at third-order and beyond. To address this discrepancy, a novel coupling approach was employed to generate random time-histories of directionally spread seas that are phase-aligned for increasing sea-state steepnesses. This data was generated both experimentally and numerically; the latter using linear and second-order random wave theory. Taking advantage of this coupling, the total population of the largest (1%) waves was sub-divided into two smaller populations of non-breaking and breaking waves. When the average profiles of the breaking and non-breaking waves are examined separately it was shown that they develop opposite asymmetries. In many sea-states these two asymmetries effectively cancel out. When the total population of large waves is considered, this produces a symmetric wave profile and the inappropriate conclusion that a weakly nonlinear QD-wave profile is relevant. Interestingly, the asymmetric profile observed for the largest non-breaking waves has the same characteristics as that of nonlinear focused waves. Importantly, the higher-order nonlinear wave-wave interactions that have been shown to produce significant amplifications in crest height statistics (Karmpadakis et al. 2019) have been shown to induce characteristic changes in the shape of the largest non-breaking waves; a result that has not previously been established from random wave records.

The coupling of the phase-aligned data has also allowed the tracking of (the same) individual waves in sea-states of different steepnesses. This has shown that the largest waves arising in a linear (or second-order) simulation do not maintain their rank (as largest) in a fully nonlinear (experimental) simulation. Whilst some mobility in the probability domain was expected due to energy dissipation by wave breaking, these waves were expected to remain at the tail of the crest height (or wave height) distributions. However, the present results show that this is not the case, emphasising the importance of both nonlinear evolution (above second-order) and, particularly, wave breaking. This has clear implications in the consideration of extremal statistics of crest heights, wave heights and the associated wave shapes. Building upon this data, a first attempt is made to quantify the conditional probabilities of amplification and wave breaking based upon the magnitude of the underlying linear (or second-order) waves. Again, this emphasizes the importance of wave breaking when seeking to describe the individual waves defining the tail of the crest height distribution in steep sea-states. Further work to quantify the variation of this effect with effective water depth, directional spread and spectral bandwidth is presently on-going.

Acknowledgments. The authors are grateful to the following sponsors of the LoWiSh (Limits on Waves in Shallow Water) JIP for funding part of this research: Shell, Mærsk, BP, Total, ConocoPhillips, Exxon, Woodside and Equinor. The authors would also like to thank Shell and Mærsk for providing access to the field data, whilst confirming that the views expressed herein are entirely their own.

APPENDIX

a. Second-order interaction kernels

The second-order interaction kernels used in Equations (4-5) are given by:

$$M^{ij-} = \sum_{i=1}^{\infty} \sum_{j=1}^{\infty} \frac{a_i a_j}{4} \left[\frac{D^{ij} - (\mathbf{k}_i \cdot \mathbf{k}_j + R_i R_j)}{\sqrt{R_i R_j}} + (R_i + R_j) \right] \tag{A1}$$

and

$$M^{ij+} = \sum_{i=1}^{\infty} \sum_{j=1}^{\infty} \frac{a_i a_j}{4} \left[\frac{D^{ij+}(\mathbf{k}_i \cdot \mathbf{k}_j - R_i R_j)}{\sqrt{R_i R_j}} + (R_i + R_j) \right], \tag{A2}$$

where

$$
\begin{aligned}
D^{ij+} = & \frac{\left(\sqrt{R_i}+\sqrt{R_j}\right)\left[\sqrt{R_i}(k_j^2-R_j^2)+\sqrt{R_j}(k_i^2-R_i^2)\right]}{\left(\sqrt{R_i}+\sqrt{R_j}\right)^2-k_{ij}^+\tanh(k_{ij}^+d)} \\
& +\frac{2\left(\sqrt{R_i}+\sqrt{R_j}\right)^2(\mathbf{k}_i\cdot\mathbf{k}_j-R_iR_j)}{\left(\sqrt{R_i}-\sqrt{R_j}\right)^2-k_{ij}^+\tanh(k_{ij}^+d)},
\end{aligned} \tag{A3}
$$

and

$$
\begin{aligned}
D^{ij-} = & \frac{\left(\sqrt{R_i}-\sqrt{R_j}\right)\left[\sqrt{R_j}(k_i^2-R_i^2)-\sqrt{R_i}(k_j^2-R_j^2)\right]}{\left(\sqrt{R_i}-\sqrt{R_j}\right)^2-k_{ij}^-\tanh(k_{ij}^-d)} \\
& +\frac{2\left(\sqrt{R_i}-\sqrt{R_j}\right)^2(\mathbf{k}_i\cdot\mathbf{k}_j+R_iR_j)}{\left(\sqrt{R_i}-\sqrt{R_j}\right)^2-k_{ij}^-\tanh(k_{ij}^-d)},
\end{aligned} \tag{A4}
$$

and where

$$
k_{ij}^- = |\mathbf{k}_i-\mathbf{k}_j|, \qquad k_{ij}^+ = |\mathbf{k}_i+\mathbf{k}_j|, \qquad R_i = k_i\tanh(k_id). \tag{A5}
$$

References

Adcock, T. A., and P. H. Taylor, 2016: Non-linear evolution of uni-directional focussed wave-groups on a deep water: A comparison of models. *Applied Ocean Research*, **59**, 147–152, doi:10.1016/j.apor.2016.05.012, URL https://www.sciencedirect.com/science/article/pii/S0141118716301523.

Adcock, T. A., P. H. Taylor, and S. Draper, 2015: Nonlinear dynamics of wave-groups in random seas: Unexpected walls of water in the open ocean. *Proceedings of the Royal Society A: Mathematical, Physical and Engineering Sciences*, **471 (2184)**, doi:10.1098/rspa.2015.0660.

Arena, F., 2005: On non-linear very large sea wave groups. *Ocean Engineering*, **32 (11-12)**, 1311–1331, doi:10.1016/j.oceaneng.2004.12.002, URL https://www.sciencedirect.com/science/article/pii/S0029801805000259.

Babanin, A., 2011: *Breaking and dissipation of Ocean surface waves*. Cambridge University Press, 1–463 pp., doi:10.1017/CBO9780511736162.

Baldock, T. E., and C. Swan, 1996: Extreme waves in shallow and intermediate water depths. *Coastal Engineering*, **27 (1-2)**, 21–46, doi:10.1016/0378-3839(95)00040-2, URL http://www.sciencedirect.com/science/article/pii/0378383995000402.

Bateman, W. J., V. Katsardi, and C. Swan, 2012: Extreme ocean waves. Part I. The practical application of fully nonlinear wave modelling. *Applied Ocean Research*, **34**, 209–224, doi:10.1016/j.apor.2011.05.002, URL https://www.sciencedirect.com/science/article/pii/S0141118711000344?via{\%}3Dihub.

Battjes, J. A., and H. W. Groenendijk, 2000: Wave height distributions on shallow foreshores. *Coastal Engineering*, **40 (3)**, 161–182, doi:10.1016/S0378-3839(00)00007-7, URL http://linkinghub.elsevier.com/retrieve/pii/S0378383900000077.

Benetazzo, A., and Coauthors, 2017: On the shape and likelihood of oceanic rogue waves. *Scientific Reports*, **7 (1)**, 1–11, doi:10.1038/s41598-017-07704-9.

Boccotti, P., 1983: Some new results on statistical properties of wind waves. *Applied Ocean Research*, **5 (3)**, 134–140, URL http://www.sciencedirect.com/science/article/pii/0141118783900676.

Boccotti, P., G. Barbaro, and L. Mannino, 1993: A Field Experiment on the Mechanics of Irregular Gravity Waves. *Journal of Fluid Mechanics*, **252**, 173–186, doi:10.1017/S0022112093003714, URL https://www.cambridge.org/core/product/identifier/S0022112093003714/type/journal{_}article.

Boccotti, P. P., 2000: *Wave mechanics for ocean engineering*. Elsevier, 496 pp.

Cartwright, D. E., and M. S. Longuet-Higgins, 1956: The statistical distribution of the maxima of a random function. *Proceedings of the Royal Society of London. Series A. Mathematical and Physical Sciences*, **237 (1209)**, 212–232, doi:10.1098/rspa.1956.0173.

Cavaleri, L., F. Barbariol, A. Benetazzo, L. Bertotti, J. R. Bidlot, P. Janssen, and N. Wedi, 2016: The Draupner wave: A fresh look and the emerging view. *Journal of Geophysical Research: Oceans*, **121 (8)**, 6061–6075, doi:10.1002/2016JC011649, URL http://doi.wiley.com/10.1002/2016JC011649.

Christou, M., and K. Ewans, 2014: Field Measurements of Rogue Water Waves. *Journal of Physical Oceanography*, **44 (9)**, 2317–2335, doi:10.1175/JPO-D-13-0199.1, URL http://journals.ametsoc.org/doi/abs/10.1175/JPO-D-13-0199.1.

DNV, 2010: DNV-RP-C205 Environmental Conditions and Environmental Loads. Tech. Rep. October, 9–123 pp.

Dysthe, K., H. E. Krogstad, and P. Müller, 2008: Oceanic Rogue Waves. *Annual Review of Fluid Mechanics*, **40 (1)**, 287–310, doi:10.1146/annurev.fluid.40.111406.102203, URL http://www.annualreviews.org/doi/10.1146/annurev.fluid.40.111406.102203.

Ewans, K., G. Feld, and P. Jonathan, 2014: On wave radar measurement. *Ocean Dynamics*, **(64)**, 1281–1303, doi:10.1007/s10236-014-0742-5.

Fedele, F., and F. Arena, 2005: Weakly nonlinear statistics of high random waves. *Physics of Fluids*, **17 (2)**, 1–10, doi:10.1063/1.1831311.

Fedele, F., J. Brennan, S. Ponce De León, J. Dudley, and F. Dias, 2016: Real world ocean rogue waves explained without the modulational instability. *Scientific Reports*, **6 (May)**, 1–11, doi:10.1038/srep27715, URL http://dx.doi.org/10.1038/srep27715.

Fernandez, L., M. Onorato, J. Monbaliu, and A. Toffoli, 2014: Modulational instability and wave amplification in finite water depth. *Natural Hazards and Earth System Sciences*, **14 (3)**, 705–711, doi:10.5194/nhess-14-705-2014.

Forristall, G. Z., 2000: Wave Crest Distributions: Observations and Second-Order Theory. *Journal of Physical Oceanography*, **30 (8)**, 1931–1943, doi:10.1175/1520-0485(2000)030⟨1931:WCDOAS⟩2.0.CO;2.

Gemmrich, J., and J. Thomson, 2017: Observations of the shape and group dynamics of rogue waves. *Geophysical Research Letters*, **44 (4)**, 1823–1830, doi:10.1002/2016GL072398.

Gibbs, R. H., and P. H. Taylor, 2005: Formation of walls of water in 'fully' nonlinear simulations. *Applied Ocean Research*, **27 (3)**, 142–157, doi:10.1016/j.apor.2005.11.009, URL https://www.sciencedirect.com/science/article/pii/S0141118705000556.

Gibson, R., M. Christou, and G. Feld, 2014: The statistics of wave height and crest elevation during the December 2012 storm in the North Sea. *Ocean Dynamics*, **64 (9)**, 1305–1317, doi:10.1007/s10236-014-0750-5, URL http://link.springer.com/10.1007/s10236-014-0750-5.

Gibson, R. S., C. Swan, and P. S. Tromans, 2007: Fully Nonlinear Statistics of Wave Crest Elevation Calculated Using a Spectral Response Surface Method: Applications to Unidirectional Sea States. *Journal of Physical Oceanography*, **37 (1)**, 3–15, doi:10.1175/JPO2956.1, URL http://journals.ametsoc.org/doi/abs/10.1175/JPO2956.1.

Guedes Soares, C., Z. Cherneva, and E. M. Antao, 2004: Steepness and asymmetry of the largest waves in storm sea states. *Ocean Engineering*, **31 (8-9)**, 1147–1167, doi:10.1016/j.oceaneng.2003.10.014.

Guedes Soares, C., and R. Pascoal, 2005: On the Profile of Large Ocean Waves. *Journal of Offshore Mechanics and Arctic Engineering*, **127 (4)**, 306, doi:10.1115/1.2087547, URL http://offshoremechanics.asmedigitalcollection.asme.org/article.aspx?articleid=1455920.

Haley, J. F., 2016: Fluid forcing in the crests of large ocean waves. Ph.D. thesis, Imperial College London.

Hasselmann, K., and Coauthors, 1973: Measurements of Wind-Wave Growth and Swell Decay during the Joint North Sea Wave Project (JONSWAP). *Ergnzungsheft zur Deutschen Hydrographischen Zeitschrift Reihe*, **A(8) (12)**, p.95.

Haver, S., and O. J. Andersen, 2000: Freak waves: Rare realizations of a typical population or typical realizations of a rare population? *Proceedings of the 10th (2000) International Offshore and Polar Engineering Conference, Vol Iii*, **I**, 123–130.

James, I. D., 1986: A note on the theoretical comparison of wave staffs and wave rider buoys in steep gravity waves. *Ocean Engineering*, **13 (2)**, 209–214, doi:10.1016/0029-8018(86)90028-4, URL https://www.sciencedirect.com/science/article/pii/0029801886900284.

Jensen, J. J., 1996: Second-order wave kinematics conditional on a given wave crest. *Applied Ocean Research*, **18 (2-3)**, 119–128, doi:10.1016/0141-1187(96)00008-9, URL https://www.sciencedirect.com/science/article/pii/0141118796000089.

Jensen, J. J., 2005: Conditional second-order short-crested water waves applied to extreme wave episodes. *Journal of Fluid Mechanics*, **545 (-1)**, 29–40, doi:10.1017/S0022112005006841, URL http://www.journals.cambridge.org/abstract{_}S0022112005006841.

Johannessen, T. B., and C. Swan, 2001: A laboratory study of the focusing of transient and directionally spread surface water waves. *Proceedings of the Royal Society A: Mathematical,* *Physical and Engineering Sciences*, **457 (2008)**, 971–1006, doi:10.1098/rspa.2000.0702, URL http://rspa.royalsocietypublishing.org/content/457/2008/971.short.

Johannessen, T. B., and C. Swan, 2003: On the nonlinear dynamics of wave groups produced by the focusing of surface-water waves. *Proceedings of the Royal Society A: Mathematical, Physical and Engineering Sciences*, **459 (2032)**, 1021–1052, doi:10.1098/rspa.2002.1028, URL http://rspa.royalsocietypublishing.org/cgi/doi/10.1098/rspa.2002.1028http://rspa.royalsocietypublishing.org/content/459/2032/1021.short.

Jonathan, P., and P. H. Taylor, 1997: On Irregular, Nonlinear Waves in a Spread Sea. *Journal of Offshore Mechanics and Arctic Engineering*, **119 (1)**, 37, doi:10.1115/1.2829043.

Karmpadakis, I., 2019: Wave Statistics in Intermediate and Shallow Water Depths. Phd thesis, Imperial College London.

Karmpadakis, I., C. Swan, and M. Christou, 2019: Laboratory investigation of crest height statistics in intermediate water depths. *Proceedings of the Royal Society A: Mathematical, Physical and Engineering Sciences*, **475 (2229)**, 20190 183, doi:10.1098/rspa.2019.0183, URL https://royalsocietypublishing.org/doi/10.1098/rspa.2019.0183.

Karmpadakis, I., C. Swan, and M. Christou, 2020: Assessment of wave height distributions using an extensive field database. *Coastal Engineering*, **157**, 103 630, doi:https://doi.org/10.1016/j.coastaleng.2019.103630.

Katsardi, V., L. de Lutio, and C. Swan, 2013: An experimental study of large waves in intermediate and shallow water depths. Part I: Wave height and crest height statistics. *Coastal Engineering*, **73**, 43–57, doi:10.1016/j.coastaleng.2012.09.007, URL http://dx.doi.org/10.1016/j.coastaleng.2012.09.007.

Katsardi, V., and C. Swan, 2011: The evolution of large non-breaking waves in intermediate and shallow water. I. Numerical calculations of uni-directional seas. *Proceedings of the Royal Society A: Mathematical, Physical and Engineering Sciences*, **467 (2127)**, 778–805, doi:10.1098/rspa.2010.0280.

Kharif, C., and E. Pelinovsky, 2003: Physical mechanisms of the rogue wave phenomenon. *European Journal of Mechanics, B/Fluids*, **22**, 603–634, doi:10.1016/j.euromechflu.2003.09.002.

Latheef, M., and C. Swan, 2013: A laboratory study of wave crest statistics and the role of directional spreading. *Proceedings of the Royal Society A: Mathematical, Physical and Engineering Sciences*, **469 (2152)**, 20120 696–20120 696, doi:10.1098/rspa.2012.0696, URL http://rspa.royalsocietypublishing.org/cgi/doi/10.1098/rspa.2012.0696.

Latheef, M., C. Swan, and J. Spinneken, 2017: A laboratory study of nonlinear changes in the directionality of extreme seas. doi:10.1098/rspa.2016.0290.

Lenain, L., and W. K. Melville, 2017: Measurements of the directional spectrum across the equilibrium saturation ranges of wind-generated surface waves. *Journal of Physical Oceanography*, **47 (8)**, 2123–2138, doi:10.1175/JPO-D-17-0017.1.

Lindgren, G., 1970: Some properties of a normal process near a local maximum. *The Annals of Mathematical Statistics*, **41 (6)**, 1870–1883, doi:10.1214/aoms/1177733256.

Lindgren, G., 1972: Local maxima of Gaussian fields. *Arkiv för matematik*, **10 (1-2)**, 195–218, doi:10.1007/BF02384809.

Longuet-Higgins, M. S., and R. W. Stewart, 1960: Changes in the form of short gravity wave and tidal currents. *Journal of Fluid Mechanics*, **8**, 565–583.

Ma, L., and C. Swan, 2020: An experimental study of wave-in-deck loading and its dependence on the properties of the incident waves. *Journal of Fluids and Structures*, **92**, 102 784, doi:10.1016/j.jfluidstructs.2019.102784, URL https://www.sciencedirect.com/science/article/pii/S0889974619301264.

Magnusson, A. K., M. A. Donelan, and W. M. Drennan, 1999: On estimating extremes in an evolving wave field. *Coastal Engineering*, **36 (2)**, 147–163, doi:10.1016/S0378-3839(99)00004-6, URL https://www.sciencedirect.com/science/article/pii/S0378383999000046.

Masterton, S. R., and C. Swan, 2008: On the accurate and efficient calibration of a 3D wave basin. *Ocean Engineering*, **35**, 763–773, doi:10.1016/j.oceaneng.2008.02.002.

Miles, M. D., and E. R. Funke, 1989: A Comparison of Methods for Synthesis of Directional Seas. *Journal of Offshore Mechanics and Arctic Engineering*, **111 (February 1989)**, 43, doi:10.1115/1.3257137.

Myrhaug, D., and S. P. Kjeldsen, 1986: Steepness and asymmetry of extreme waves and the highest waves in deep water. *Ocean Engineering*, **13 (6)**, 549–568, doi:10.1016/0029-8018(86)90039-9, URL https://www.sciencedirect.com/science/article/pii/0029801886900399.

Nikolkina, I., and I. Didenkulova, 2011: Rogue waves in 20062010. *Natural Hazards and Earth System Sciences*, **11 (11)**, 2913–2924, doi:10.5194/nhess-11-2913-2011, URL https://www.nat-hazards-earth-syst-sci.net/11/2913/2011/.

Ochi, M. K., 1998: *Ocean Waves : the Stochastic Approach*. Cambridge University Press, 332 pp.

Onorato, M., and Coauthors, 2009: Statistical properties of mechanically generated surface gravity waves: A laboratory experiment in a three-dimensional wave basin. *Journal of Fluid Mechan-*

ics, **627**, 235–257, doi:10.1017/S002211200900603X, URL http://www.journals.cambridge.org/abstract{_}S002211200900603X.

Perlin, M., W. Choi, and Z. Tian, 2013: Breaking Waves in Deep and Intermediate Waters. *Annual Review of Fluid Mechanics*, **45 (1)**, 115–145, doi:10.1146/annurev-fluid-011212-140721, URL http://www.annualreviews.org/doi/10.1146/annurev-fluid-011212-140721.

Phillips, O. M., D. Gu, and M. Donelan, 1993a: Expected Structure of Extreme Waves in a Gaussian Sea. Part I: Theory and SWADE Buoy Measurements. *Journal of Physical Oceanography*, **23 (5)**, 992–1000, doi:10.1175/1520-0485(1993)023⟨0992:esoewi⟩2.0.co;2.

Phillips, O. M., D. Gu, and E. J. Walsh, 1993b: On the Expected Structure of Extreme Waves in a Gaussian Sea. Part II: SWADE Scanning Radar Altimeter Measurements. *Journal of Physical Oceanography*, **23 (10)**, 2297–2309, doi:10.1175/1520-0485(1993)023⟨2297:otesoe⟩2.0.co;2, URL http://journals.ametsoc.org/doi/abs/10.1175/1520-0485{\%}281993{\%}29023{\%}3C2297{\%}3AOTESOE{\%}3E2.0.CO{\%}3B2.

Santo, H., P. H. Taylor, R. Eatock Taylor, and Y. S. Choo, 2013: Average Properties of the Largest Waves in Hurricane Camille. *Journal of Offshore Mechanics and Arctic Engineering*, **135 (1)**, 011 602, doi:10.1115/1.4006930, URL http://offshoremechanics.asmedigitalcollection.asme.org/article.aspx?doi=10.1115/1.4006930.

Sharma, J., and R. G. Dean, 1981: Second-Order Directional Seas and Associated Wave Forces. *Society of Petroleum Engineers Journal*, **21 (1)**, 129–140, doi:10.2118/8584-PA.

Shemer, L., A. Sergeeva, and D. Liberzon, 2010: Effect of the initial spectrum on the spatial evolution of statistics of unidirectional nonlinear random waves. *Journal of Geophysical Research: Oceans*, **115 (12)**, 1–12, doi:10.1029/2010JC006326.

Slunyaev, A., C. Kharif, E. Pelinovsky, and T. Talipova, 2002: Nonlinear wave focusing on water of finite depth. *Physica D: Nonlinear Phenomena*, **173 (1-2)**, 77–96, doi:10.1016/S0167-2789(02)00662-0.

Spinneken, J., and C. Swan, 2012: The operation of a 3D wave basin in force control. *Ocean Engineering*, **55**, 88–100, doi:10.1016/j.oceaneng.2012.07.024, URL http://dx.doi.org/10.1016/j.oceaneng.2012.07.024.

Stansell, P., J. Wolfram, and B. Linfoot, 2002: Effect of sampling rate on wave height statistics. *Ocean Engineering*, **29 (9)**, 1023–1047, doi:10.1016/S0029-8018(01)00066-X.

Tayfun, M. A., 1993: SamplingRate Errors in Statistics of Wave Heights and Periods. 172–192 pp., doi:10.1061/(ASCE)0733-950X(1993)119:2(172).

Tayfun, M. A., 2006a: Statistics of nonlinear wave crests and groups. *Ocean Engineering*, **33 (11-12)**, 1589–1622, doi:10.1016/j.oceaneng.2005.10.007.

Tayfun, M. A., 2006b: Statistics of nonlinear wave crests and groups. *Ocean Engineering*, **33 (11-12)**, 1589–1622, doi:10.1016/j.oceaneng.2005.10.007, URL https://www.sciencedirect.com/science/article/pii/S0029801805002581.

Tayfun, M. A., and F. Fedele, 2007: Expected shape of extreme waves in storm seas. *Proceedings of the International Conference on Offshore Mechanics and Arctic Engineering - OMAE*, **2 (1)**, 53–60, doi:10.1115/OMAE2007-29073, URL http://www.scopus.com/inward/record.url?eid=2-s2.0-37149009877{\&}partnerID=40.

Taylor, P. H., and B. A. Williams, 2004: Wave Statistics for Intermediate Depth Water-NewWaves and Symmetry. *Journal of Offshore Mechanics and Arctic Engineering*, Vol. 126, 54, doi:10.1115/1.1641796, URL http://offshoremechanics.asmedigitalcollection.asme.org/article.aspx?articleid=1455120.

Tromans, P. S., A. R. Anatruk, and P. Hagemeijer, 1991: New Model for the Kinematics of Large Ocean Waves Application as a Design Wave. *Proceedings of the First International Offshore and Polar Engineering Conference*, **8 (August)**, 64–71.

Walker, D. A., P. H. Taylor, and R. E. Taylor, 2004: The shape of large surface waves on the open sea and the Draupner New Year wave. *Applied Ocean Research*, **26 (3-4)**, 73–83, doi:10.1016/j.apor.2005.02.001.

Whittaker, C. N., A. C. Raby, C. J. Fitzgerald, and P. H. Taylor, 2016: The average shape of large waves in the coastal zone. *Coastal Engineering*, **114**, 253–264, doi:10.1016/j.coastaleng.2016.04.009, URL http://dx.doi.org/10.1016/j.coastaleng.2016.04.009, arXiv:1408.1149.

LIST OF TABLES

TABLE 1. Definition of the laboratory test cases at Imperial College London ($d = 0.5\,\mathrm{m}$).

Sea-state	T_p [s]	H_s [mm]	$S_p = \dfrac{2\pi H_s}{g T_p^2}$ [-]	$\dfrac{H_s k_p}{2}$ [-]	σ_θ [deg]	$k_p d$ [-]
A1	1.2	22	0.01	0.035	0,10, 20	1.53
A2		44	0.02	0.069		
A3		67	0.03	0.103		
A4		89	0.04	0.138		
A5		112	0.05	0.172		
A6		134	0.06	0.207		
A7		157	0.07	0.241		
B1	1.4	30	0.01	0.037	0,10, 20	1.22
B2		61	0.02	0.075		
B3		91	0.03	0.112		
B4		122	0.04	0.150		
B5		153	0.05	0.187		
B6		183	0.06	0.224		
C1	1.6	40	0.01	0.040	0,10, 20	1.02
C2		80	0.02	0.081		
C3		120	0.03	0.122		
C4		160	0.04	0.163		
C5		200	0.05	0.204		

LIST OF FIGURES

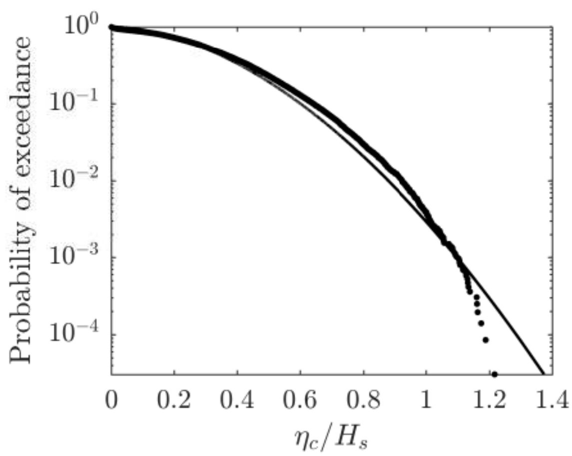

FIG. 1. Normalised crest height (η_c/H_s) distribution [dots] arising in a laboratory-generated, short-crested sea-state with $k_pd = 1.22$ and $H_s = 15.3\,\mathrm{m}$ compared to the predictions of the Forristall (2000) distribution [continuous line].

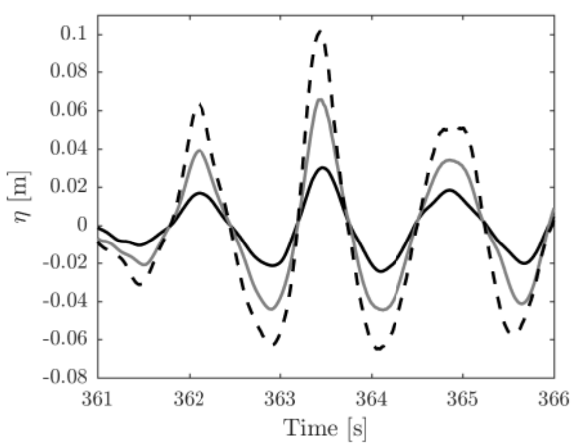

975 FIG. 2. Segment of time-histories that demonstrate the wave generation method and relate to the same seed in sea-states with: $S_p = 0.01$ [black line], $S_p = 0.02$ [grey line] and $S_p = 0.03$ [dashed line]; all with $\sigma_\theta = 10°$.

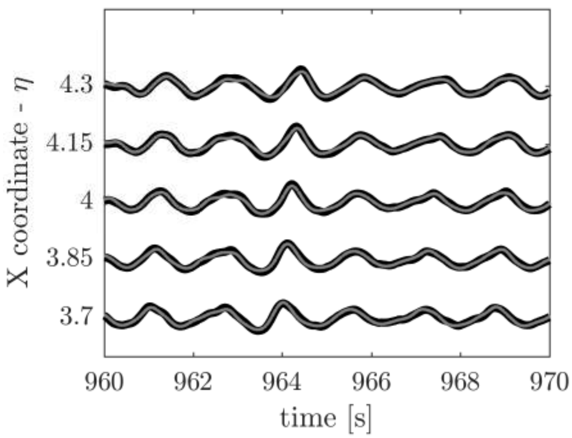

(a) $S_p : 0.01$, $k_p d : 1.02$ and $\sigma_\theta : 10°$

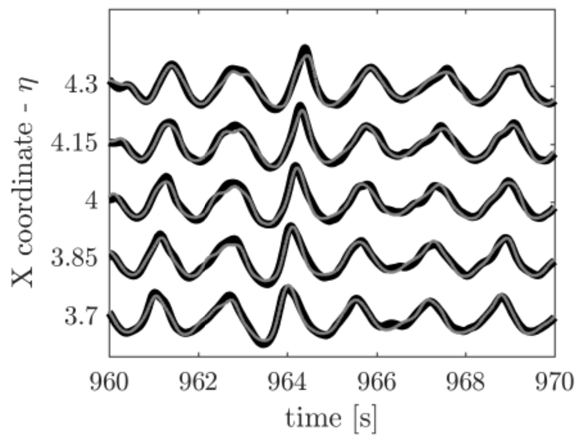

(b) $S_p : 0.02$, $k_p d : 1.02$ and $\sigma_\theta : 10°$

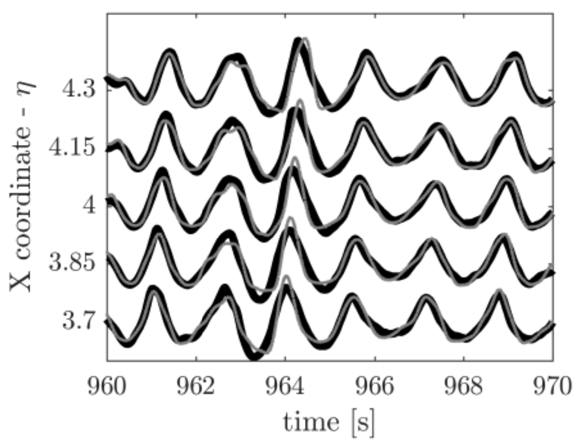

(c) $S_p : 0.03$, $k_p d : 1.02$ and $\sigma_\theta : 10°$

FIG. 3. Comparisons between the experimental [black line] and numerical (SORWT) [grey line] time-histories of the free surface elevation, $\eta(t)$, along the centreline of the wave basin; the gauge locations being indicated in the *y*-axis.

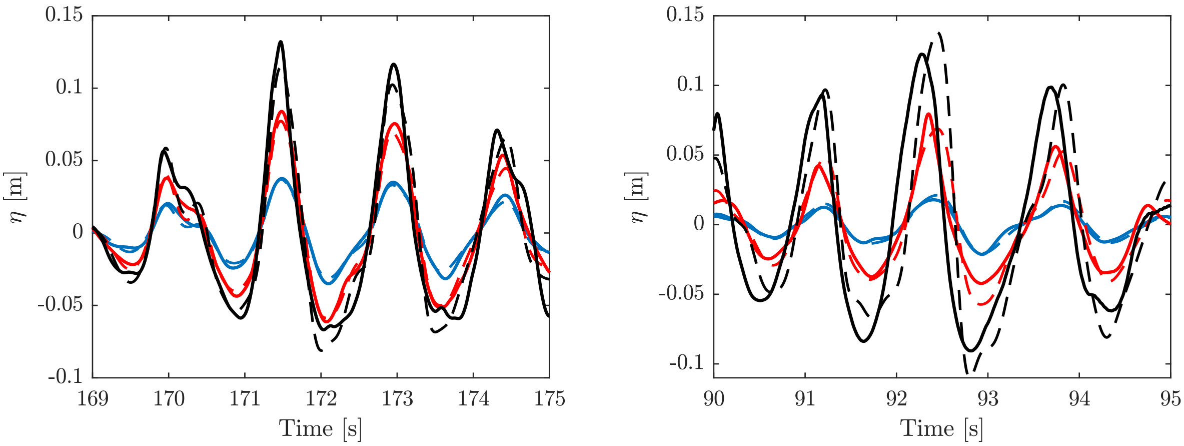

(a) $k_p d$: 1.02 and σ_θ : 10°

(b) $k_1 d$: 1.22 and σ_θ : 10°

FIG. 4. Comparison of experimental (continuous lines) and numerical (dashed lines) time-histories of water surface elevation, $\eta(t)$. The numerical results correspond to SORWT simulations using the same input parameters as the experiment. The results relate to: (a) $S_p = 0.01$ [blue line], $S_p = 0.02$ [red line] and $S_p = 0.03$ [black line] and (b) $S_p = 0.01$ [blue line], $S_p = 0.03$ [red line] and $S_p = 0.06$ [black line].

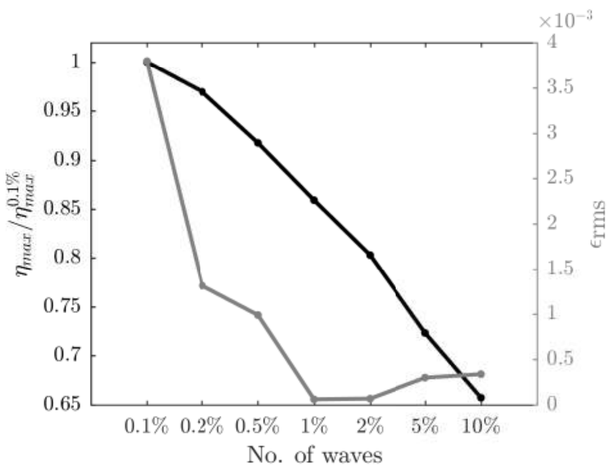

FIG. 5. Assessing the number of large wave profiles appropriate to the determination of an effective average. Left axis [black line]: ratio between the maximum crest from each average profile and the maximum crest for the smallest percentile. Right axis [grey line]: Root-mean-square error between the scaled autocorrelation function and average wave shapes; all data being based upon long linear calculations.

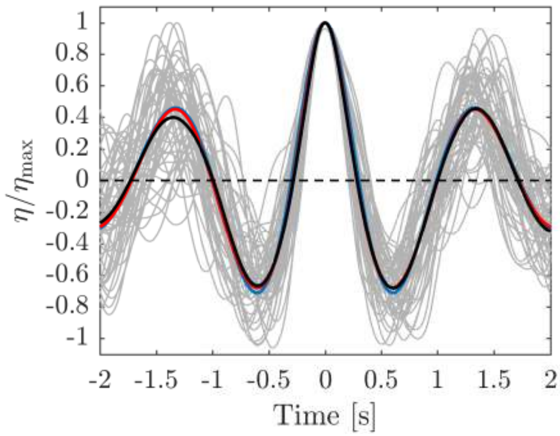

(a) Laboratory data: $S_p = 0.01$

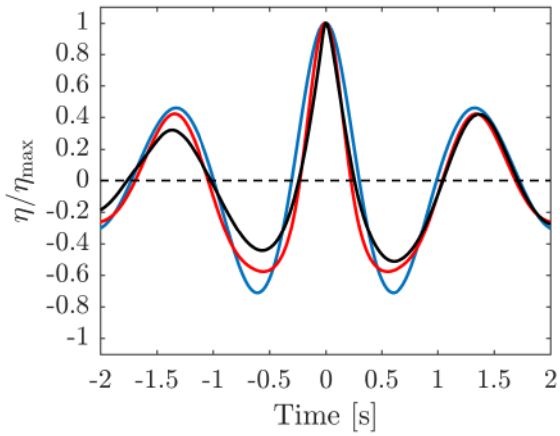

(b) Laboratory data: $S_p = 0.04$

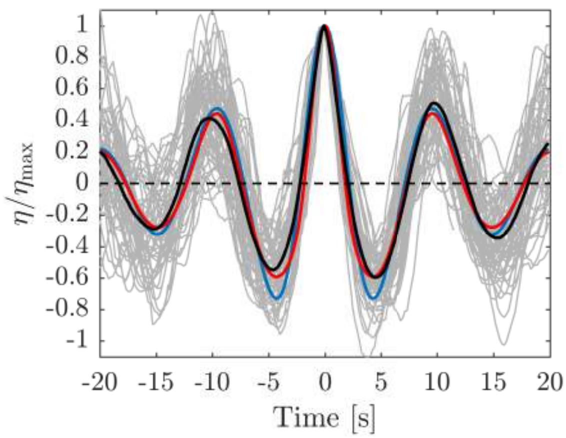

(c) Field data: $H_s = 4\,\mathrm{m}$, $T_p = 12\,\mathrm{s}$, $d = 45\,\mathrm{m}$

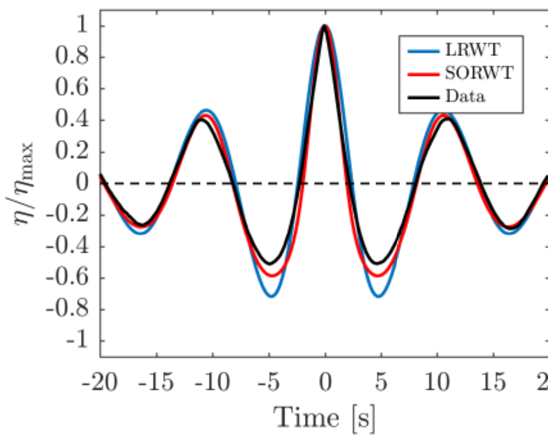

(d) Field data: $H_s = 6\,\mathrm{m}$, $T_p = 12\,\mathrm{s}$, $d = 45\,\mathrm{m}$

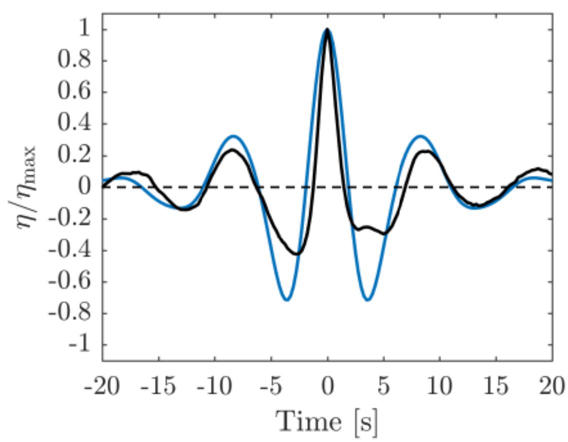

(e) Field data: $H_s = 2\,\mathrm{m}$, $T_p = 8\,\mathrm{s}$, $d = 7.7\,\mathrm{m}$

FIG. 6. Normalised linear [blue line] and second-order corrected [red line] QD-wave profiles (η/η_{max}) compared to the average shapes of the largest waves [black line] in a wide variety of sea-states; individual wave profiles being shown in gray. Sub-plots (a) and (b) correspond to experimental measurements with $k_p d = 1.22$ and $\sigma_\theta = 10^\circ$ but different steepnesses. Sub-plots (c)-(e) correspond to sea-states recorded in the field.

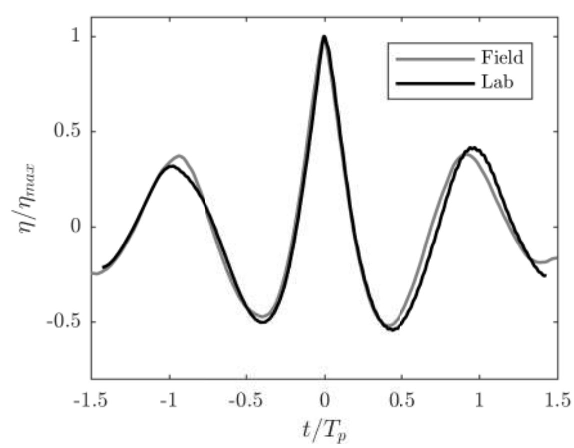

FIG. 7. Normalised average profiles of the largest waves (η/η_{max}) showing agreement between field and laboratory data with similar sea-state characteristics ($k_p d = 1.22$, $S_p = 0.03$). The field data have been recorded at a water depth of $d = 45\,\text{m}$, while the experimental data correspond to case B3 with $\sigma_\theta = 10°$.

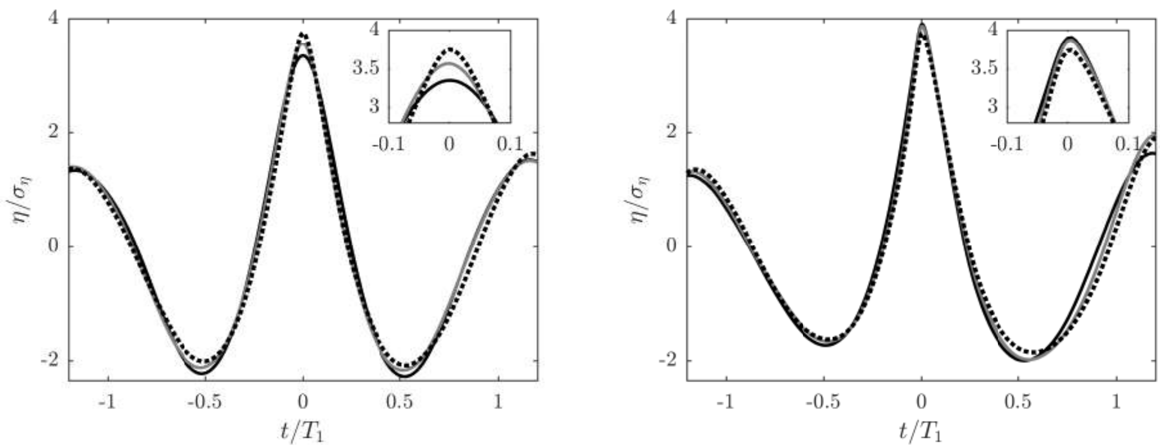

(a) $0.01 \leq S_p \leq 0.03$ (b) $0.04 \leq S_p \leq 0.06$

FIG. 8. Effect of increasing sea-state steepness (as a measure of nonlinearity) for the largest 1% of experimentally recorded waves. The average wave profiles (η/σ_η) correspond to: (a) $S_p = 0.01$ [black line], $S_p = 0.02$ [grey line] and $S_p = 0.03$ [dotted line] and (b) $S_p = 0.04$ [black line], $S_p = 0.05$ [grey line] and $S_p = 0.06$ [dotted line]; all with $k_p d = 1.22$ and $\sigma_\theta = 10°$.

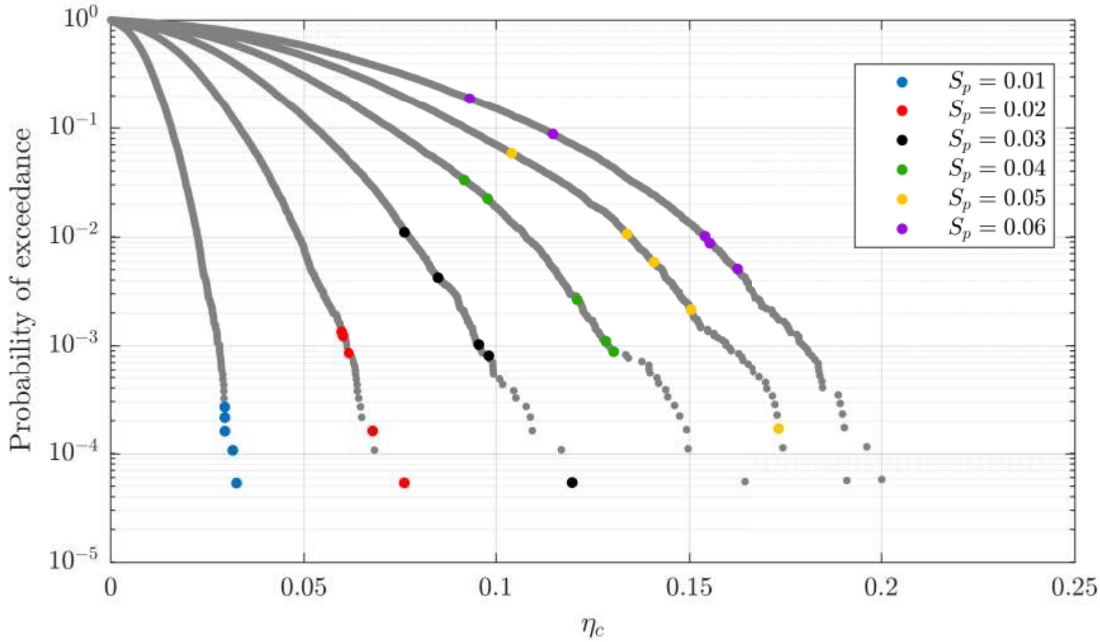

FIG. 9. Crest height distributions (η_c) [grey dots] arising in all the sea-states with $k_p d = 1.22$ and $\sigma_\theta = 10°$; the 5 largest crest heights in the corresponding SORWT simulations [coloured dots] being tracked for increasing sea-state steepness.

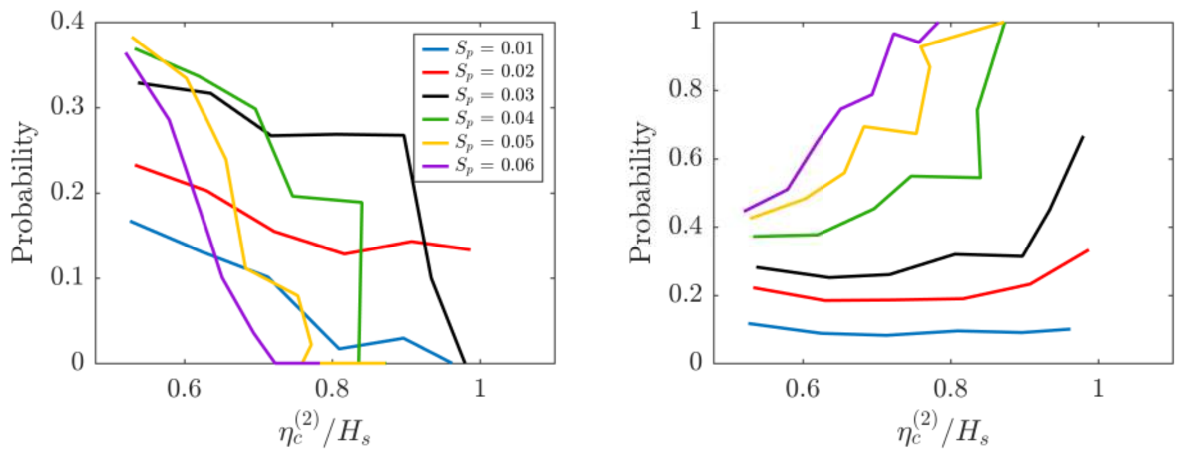

(a) Probability of wave amplification.

(b) Probability of wave breaking.

FIG. 10. Probability of waves being (a) amplified or (b) breaking conditional on their corresponding normalised SORWT crest height ($\eta_c^{(2)}/H_s$) for all sea-states with $k_p d = 1.22$ and $\sigma_\theta = 10°$.

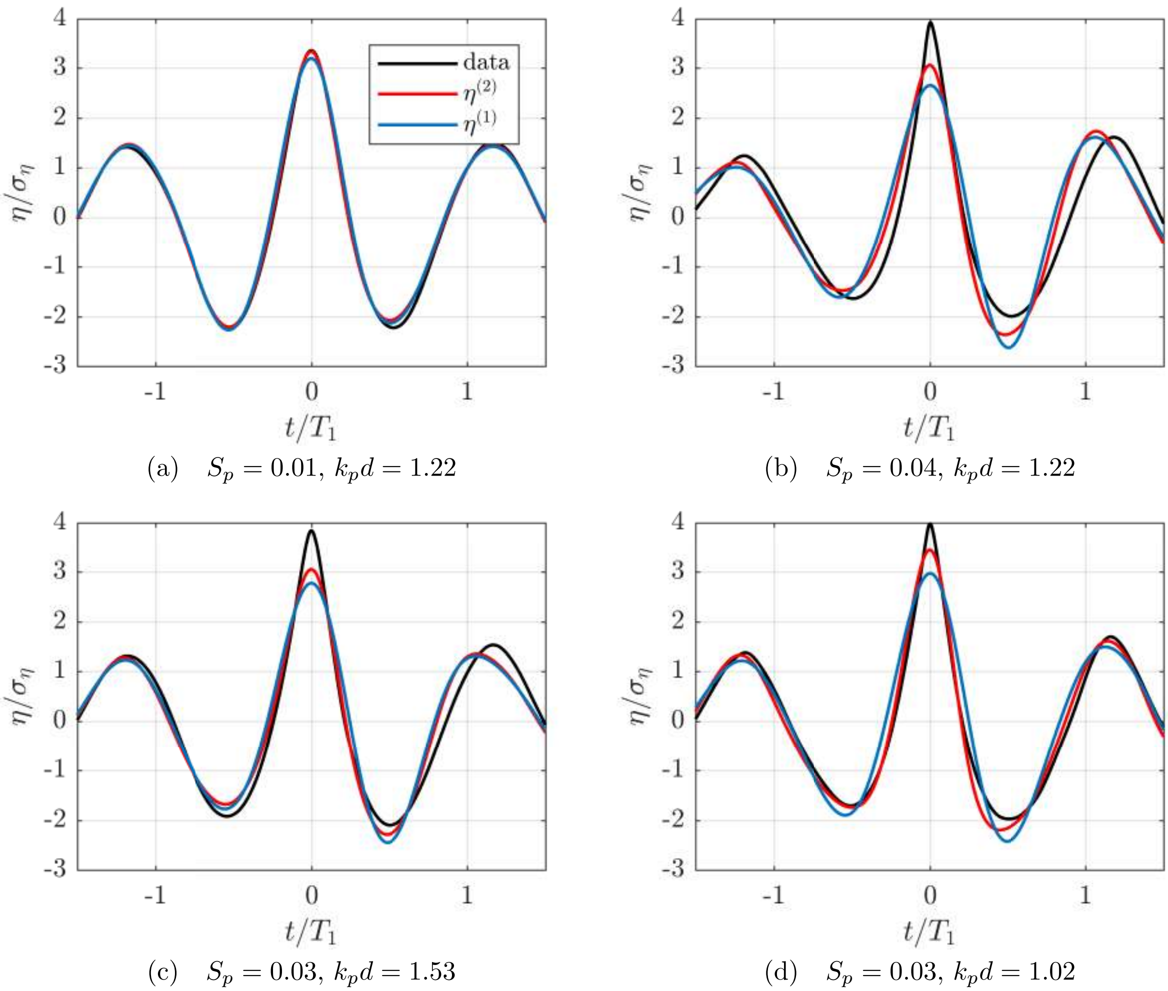

(a) $S_p = 0.01$, $k_p d = 1.22$

(b) $S_p = 0.04$, $k_p d = 1.22$

(c) $S_p = 0.03$, $k_p d = 1.53$

(d) $S_p = 0.03$, $k_p d = 1.02$

FIG. 11. Effects of nonlinear amplification on the average shape of non-breaking waves. The measured profiles [black] are compared to their corresponding SORWT ($\eta^{(2)}$) [red] and linear ($\eta^{(1)}$) [blue] profiles. The sub-plots correspond to cases with different $k_p d$ and S_p, all with $\sigma_\theta = 10^\circ$.

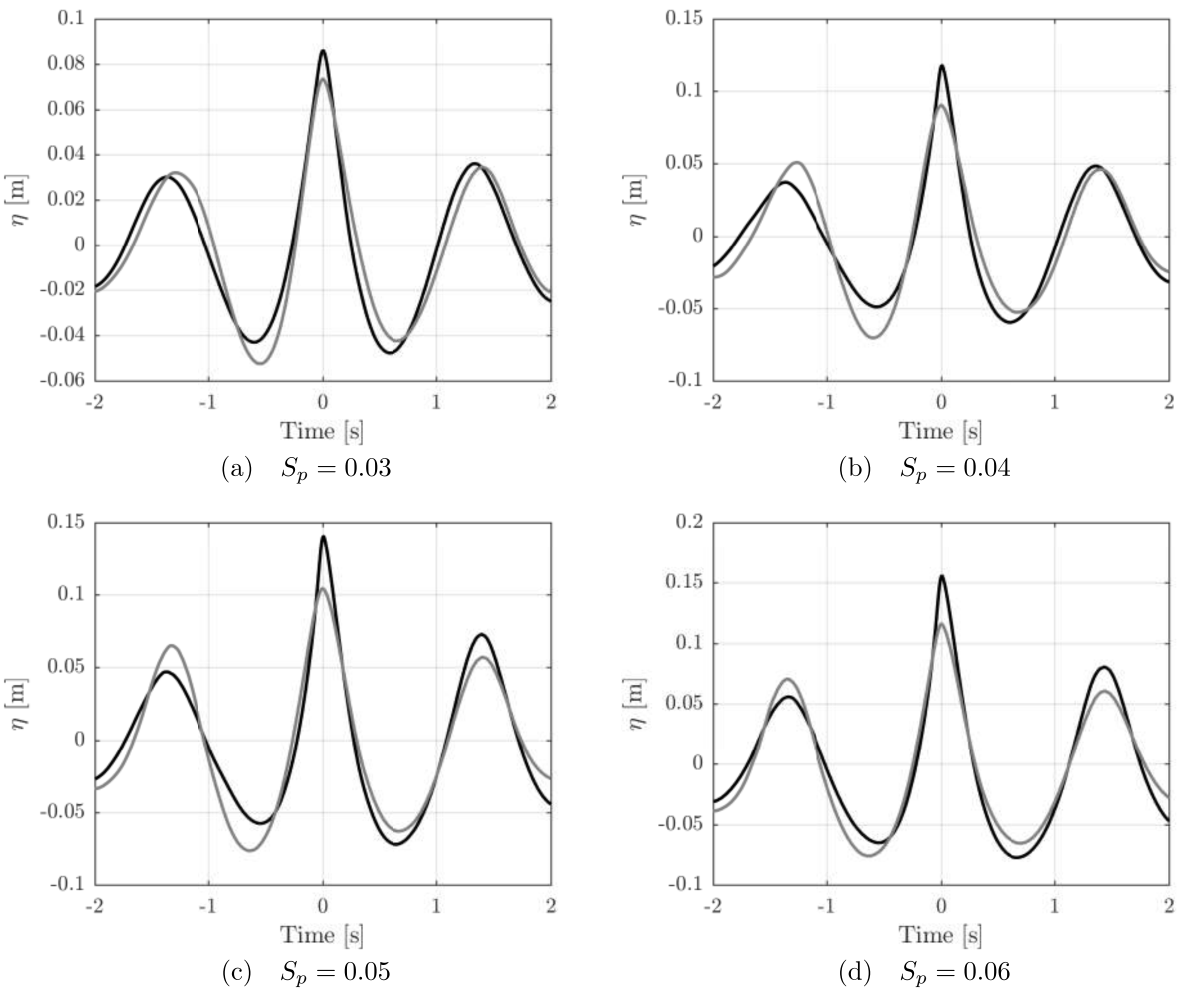

(a) $S_p = 0.03$ (b) $S_p = 0.04$

(c) $S_p = 0.05$ (d) $S_p = 0.06$

FIG. 12. The competing effects of nonlinear amplifications and wave breaking on the average wave profiles. Comparison between average profiles of non-breaking and breaking waves for varying sea-state steepness and ($k_p d = 1.22$, $\sigma_\theta = 10°$): Large non-breaking waves [black line], large breaking waves [grey line].

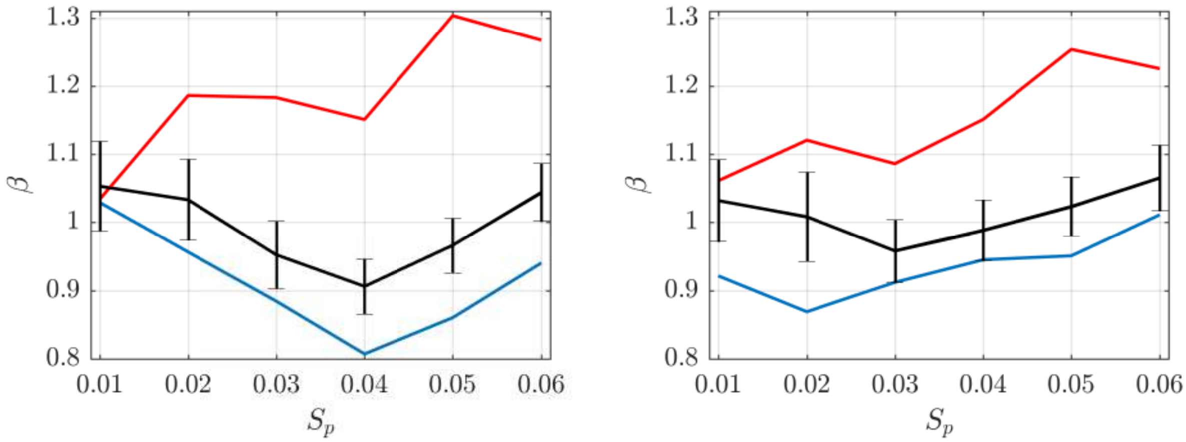

(a) $k_p d = 1.22$ and $\sigma_\theta = 10°$ (b) $k_p d = 1.22$ and $\sigma_\theta = 20°$

FIG. 13. Evolution of the asymmetry parameter β with increasing sea-state steepness S_p. The results correspond to the total population [black line] (of the 1%) of largest waves, the non-breaking [blue line] and breaking [red line] populations. The 95% confidence intervals have been added on the estimates for the total population.

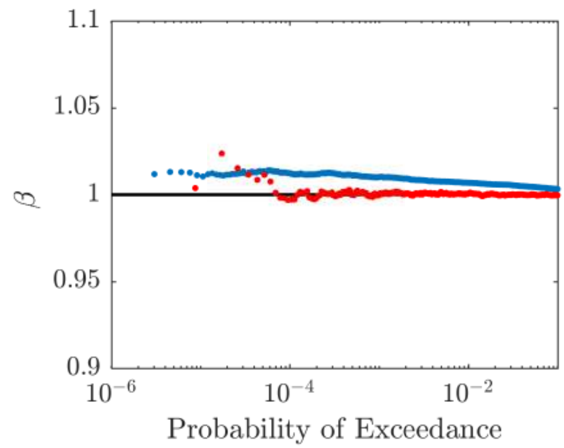

1013 FIG. 14. Distribution of the front-back wave trough ratio (β) corresponding to all sorted wave heights arising

1014 in field measurements water depths of $d = 45\,\mathrm{m}$ [red] and $d = 7.7\,\mathrm{m}$ [blue].